

TEMPERATURE STRUCTURE AND ATMOSPHERIC CIRCULATION OF DRY, TIDALLY LOCKED ROCKY EXOPLANETS

DANIEL D. B. KOLL AND DORIAN S. ABBOT

Department of the Geophysical Sciences, University of Chicago, Chicago, IL 60637

ABSTRACT

Next-generation space telescopes will observe the atmospheres of rocky planets orbiting nearby M-dwarfs. Understanding these observations will require well-developed theory in addition to numerical simulations. Here we present theoretical models for the temperature structure and atmospheric circulation of dry, tidally locked rocky exoplanets with grey radiative transfer and test them using a general circulation model (GCM). First, we develop a radiative-convective model that captures surface temperatures of slowly rotating and cool atmospheres. Second, we show that the atmospheric circulation acts as a global heat engine, which places strong constraints on large-scale wind speeds. Third, we develop a radiative-convective-subsiding model which extends our radiative-convective model to hot and thin atmospheres. We find that rocky planets develop large day-night temperature gradients at a ratio of wave-to-radiative timescales up to two orders of magnitude smaller than the value suggested by work on hot Jupiters. The small ratio is due to the heat engine inefficiency and asymmetry between updrafts and subsidence in convecting atmospheres. Fourth, we show using GCM simulations that rotation only has a strong effect on temperature structure if the atmosphere is hot or thin. Our models let us map out atmospheric scenarios for planets such as GJ 1132b and show how thermal phase curves could constrain them. Measuring phase curves of short-period planets will require similar amounts of time on the *James Webb Space Telescope* as detecting molecules via transit spectroscopy, so future observations should pursue both techniques.

1. INTRODUCTION

1.1. *Importance of atmospheric dynamics*

Terrestrial exoplanets orbiting M-dwarfs are extremely common. Results from the *Kepler* space telescope show that there are at least ~ 0.5 rocky planets per M-dwarf, half of which could even be habitable (Dressing & Charbonneau 2015). Just as important, near-future telescopes like the *James Webb Space Telescope* (*JWST*) will be able to characterize the atmospheres of these planets (Deming et al. 2009; Beichman et al. 2014; Cowan et al. 2015), making them one of the most promising observational targets of the coming decade.

New theories are needed to understand the potential atmospheres of these exoplanets, particularly their temperature structures and large-scale circulations. An atmosphere's temperature structure and circulation critically influence a planet's surface and atmospheric evolution as well as its potential habitability (Kasting 1988; Abe et al. 2011; Yang et al. 2013). An atmosphere's temperature structure and circulation are also important for interpreting observations. For example, a planet's emission spectrum is determined by the vertical temperature distribution of its atmosphere, while the planet's thermal and optical phase curves are set by its day-night temperature gradient and cloud patterns (Seager & Deming 2009; Yang et al. 2013; Hu et al. 2015). Even transit measurements can be strongly influenced by chemical mixing and clouds, which in turn depend on the atmosphere's large-scale circulation (Fortney 2005; Parmentier et al. 2013; Charnay et al. 2015; Line & Parmentier 2016).

Unfortunately there is a large gap between current theories of terrestrial atmospheres and the wide range of potential exoplanets. Planets accessible to follow-up observations will generally be in short-period orbits, experience strong tidal forces, and thus tend to be either tidally locked or captured in higher spin-orbit resonances (Kasting et al. 1993; Makarov et al. 2012). The solar system offers no direct analogs of such atmospheres, and their dynamics

are still poorly understood. In this work we focus on tidally locked (synchronously rotating) atmospheres because their dynamics would differ most drastically from rapidly rotating atmospheres, whereas planets in higher spin-orbit resonances should resemble hybrids between tidally locked and rapidly rotating planets (also see Section 9).

1.2. Previous work and open questions

Many groups have already used general circulation models (GCMs) to study the thermal structure and atmospheric circulation of tidally locked terrestrial planets (e.g., [Joshi et al. 1997](#); [Merlis & Schneider 2010](#); [Heng et al. 2011](#); [Pierrehumbert 2011a](#); [Selsis et al. 2011](#); [Leconte et al. 2013](#); [Yang et al. 2013](#); [Zalucha et al. 2013](#); [Wordsworth 2015](#); [Kopparapu et al. 2016](#)). These studies investigated a range of processes that shape the atmospheres of tidally locked planets, including the large-scale day-night circulation, equatorial superrotation, heat transport by atmospheric waves, and the potential for atmospheric collapse if the nightside becomes too cold. The development of theory to understand these processes, however, has not kept up with the rapid proliferation of simulations.

Recent theories of rocky planets focused on planets for which the horizontal heat redistribution is extremely efficient ([Pierrehumbert 2011a](#); [Mills & Abbot 2013](#); [Yang & Abbot 2014](#); [Wordsworth 2015](#)). Among the latter, [Pierrehumbert \(2011b\)](#) developed a scaling relation for the surface temperature of a planet that is horizontally completely uniform and whose atmosphere is optically thick,

$$T_s = T_{eq} \times \frac{\tau_{LW}^\beta}{\Gamma(1 + 4\beta)^{1/4}}. \quad (1)$$

Here T_{eq} is the planet's equilibrium temperature defined as $T_{eq} \equiv [L_*(1 - \alpha)/(4\sigma)]^{1/4}$, τ_{LW} is the longwave optical thickness, Γ is the Gamma function defined as $\Gamma(a) \equiv \int_0^\infty t^{a-1} \exp(-t) dt$, and $\beta \equiv R/(c_p n)$. L_* is the stellar constant, α is the planetary bond albedo, σ is the Stefan-Boltzmann constant, R is the specific gas constant, c_p is the specific heat capacity, and n governs how optical thickness depends on pressure (Section 2). Similarly, [Wordsworth \(2015\)](#) developed a theory for the temperature structure of tidally locked atmospheres in the optically thin limit, in which atmospheres become particularly vulnerable to atmospheric collapse. [Wordsworth \(2015\)](#) found a lower bound for the nightside temperature of a tidally locked planet¹,

$$T_n = T_{eq} \left(\frac{\tau_{LW}}{2} \right)^{1/4}. \quad (2)$$

Common to both scalings is that they are not valid in the physically important regime of optical depth unity, and indeed contradict each other when extrapolated to this limit. Neither do they explicitly account for horizontal atmospheric dynamics². Nevertheless, we expect that the dynamics of tidally locked planets should be sensitive to a range of additional processes, including the atmosphere's radiative timescale, surface drag, and planetary rotation, all of which have not yet been addressed for rocky exoplanets.

On a different front, recent work has begun to understand the atmospheric circulation of hot Jupiters ([Perez-Becker & Showman 2013](#); [Showman et al. 2015](#); [Komacek & Showman 2016](#)). [Perez-Becker & Showman \(2013\)](#) developed a weak-temperature-gradient (WTG) theory that explains why the hottest hot Jupiters also tend to have the highest day-night brightness temperature contrasts. WTG describes atmospheres that are slowly rotating and are relatively cool, which allows atmospheric waves to efficiently eliminate horizontal temperature gradients ([Showman et al. 2013](#)). In equilibrium the wave adjustment leads to subsidence, that is, sinking motions, in regions of radiative cooling (see Section 5). [Perez-Becker & Showman \(2013\)](#) showed that day-night temperature gradients become large once the radiative timescale becomes shorter than the timescale for subsidence, $t_{rad} \lesssim t_{sub}$. On hot Jupiters with sufficiently strong drag, temperature gradients are large when

$$t_{rad} \lesssim \frac{t_{wave}}{t_{drag}} \times t_{wave}, \quad (3)$$

where t_{wave} is the timescale for a gravity wave to horizontally propagate across the planet and t_{drag} is a characteristic drag timescale.

It would be tempting to assume Equation 3 applies equally well to rocky exoplanets. That is not the case, and published GCM results of rocky planets are already at odds with it. We show in Appendix A that for most tidally locked terrestrial planets drag and wave timescales are comparable, $t_{drag} \approx t_{wave}$. If Equation 3 applied to rocky

¹ We use Equation 2 instead of Equation (29) in [Wordsworth \(2015\)](#), because it does not assume a specific value for n .

² [Wordsworth \(2015\)](#) also developed a model that incorporates dynamics, which we revisit in Section 4.

planets, they should develop large day-night temperature gradients when

$$1 \lesssim \frac{t_{wave}}{t_{rad}}. \quad (4)$$

In contrast, the GCM simulations in [Selsis et al. \(2011\)](#) indicate that tidally locked rocky planets can develop atmospheric temperature gradients at a surface pressure of about 1 bar (their Fig. 5), which translates to a much lower value of $t_{wave}/t_{rad} \sim 0.05$. Similarly, we found in [Koll & Abbot \(2015\)](#) that rocky exoplanets develop large day-night brightness temperature contrasts when $t_{wave}/t_{rad} \gtrsim 10^{-2}$. The disagreement between hot Jupiter theory and rocky planets has not been explored yet. Here we will show that the qualitative threshold for a WTG atmosphere to develop large temperature gradients, $t_{rad} \lesssim t_{sub}$, also applies to rocky planets. However, rocky planets end up behaving quite differently than hot Jupiters because of the processes that determine the large-scale circulation and the subsidence timescale t_{sub} .

1.3. Outline

In this paper we develop a series of models to understand the atmospheres of tidally locked rocky exoplanets. To show how our models complement previous theories we adopt our nondimensional analysis from [Koll & Abbot \(2015\)](#). Using the Buckingham-Pi theorem ([Buckingham 1914](#)), we showed that the dynamics of a dry and tidally locked atmosphere with grey radiation are governed by only six nondimensional parameters. This set of nondimensional parameters allows us to cleanly disentangle the atmospheric processes that need to be addressed. One choice for the six parameters is given by

$$\left(\frac{R}{c_p}, \frac{a^2}{L_{Ro}^2}, \frac{t_{wave}}{t_{rad}}, \tau_{SW}, \tau_{LW}, \frac{t_{wave}}{t_{drag}} \right). \quad (5)$$

The convective lapse rate is controlled by R/c_p . The nondimensional Rossby radius a^2/L_{Ro}^2 governs the influence of planetary rotation on equatorial waves. Here a is the planetary radius, the equatorial Rossby deformation radius is defined as $L_{Ro} \equiv \sqrt{ac_{wave}/(2\Omega)}$, Ω is the planetary rotation rate, and c_{wave} is the speed of a gravity wave. Although c_{wave} is a priori unknown, because it depends on an atmosphere’s vertical temperature structure, we can place a reasonable upper bound on it by assuming an isothermal atmosphere. This assumption leads to $c_{wave} = \sqrt{R/c_p} \times \sqrt{gH} = \sqrt{R/c_p} \times \sqrt{RT_{eq}}$, where g is the acceleration of gravity and $H \equiv RT_{eq}/g$ is the scale height. The wave-to-radiative timescale ratio, t_{wave}/t_{rad} , compares the time it takes for equatorial waves to redistribute energy across the planet, $t_{wave} \equiv a/c_{wave}$, to the atmosphere’s radiative cooling time, $t_{rad} \equiv c_p p_s / (g\sigma T_{eq}^3)$. The atmospheric shortwave and longwave optical thicknesses are τ_{SW} and τ_{LW} . The ratio of wave to drag timescales $t_{wave}/t_{drag} = C_D a/H$ governs surface friction and turbulent heat fluxes ([Appendix A](#)).

We only consider atmospheres that are transparent to shortwave absorption ($\tau_{SW} = 0$), which ensures that the solid surface substantially affects the atmospheric dynamics. This means we exclude from our consideration potential “rocky” planet scenarios with a bulk silicate composition, but with gaseous envelopes several hundreds of bar thick ([Owen & Mohanty 2016](#)). We expect that the observable atmospheres of such planets would resemble gas giants more than rocky planets, with dynamics that are better captured by theories developed for hot Jupiters ([Perez-Becker & Showman 2013](#); [Showman et al. 2015](#); [Komacek & Showman 2016](#)).

Of the six nondimensional parameters τ_{SW} and τ_{LW} govern radiative transfer, R/c_p sets the vertical temperature structure, and the remaining three parameters determine the horizontal dynamics. As an important starting point, we formulate an analytical radiative-convective (RC) model for the temperature structure of tidally locked atmospheres that only depends on $\beta \equiv R/(nc_p)$ and τ_{LW} and therefore addresses the first two processes ([Section 3](#)). In the optically thick regime this model reduces to the asymptotic limit found by [Pierrehumbert \(2011b\)](#). We then turn to horizontal dynamics. We show the day-night circulation acts as a heat engine, in which heating and cooling balance frictional dissipation in the dayside boundary layer ([Section 4](#)). We use our heat engine theory to develop a radiative-convective-subsiding (RCS) model that includes the effects of t_{wave}/t_{drag} and t_{wave}/t_{rad} on temperature structure ([Section 5](#)). For cool/thick atmospheres the RCS model reduces to the RC model, whereas for optically thin and hot/thin atmospheres it reduces to the asymptotic limit found by [Wordsworth \(2015\)](#). Our RCS model explains why rocky planets develop large day-night temperature gradients at a significantly lower t_{wave}/t_{rad} threshold than hot Jupiters ([Section 6](#)). Next, we use GCM simulations to address rapidly rotating planets and a^2/L_{Ro}^2 ([Section 7](#)). We find that t_{wave}/t_{rad} has to be big for rotation to have a strong effect on temperature structure, that is, cause large eastward hot spot offsets or cold nightside vortices. Our results imply that planets like GJ 1132b or HD 219134b will likely have significant day-night temperature contrasts, unless their atmospheres are dominated by H_2 ([Section 8](#)). We estimate that detecting these potential contrasts via thermal phase curves will require about as much time with *JWST* as detecting molecular

Parameter	Symbol	Unit	Minimum value	Maximum value
Planetary radius	a	a_{\oplus}	0.5	2
Rotation rate	Ω	days ⁻¹	$2\pi/100$	$2\pi/1$
Equilibrium temperature	T_{eq}	K	250	600
Surface gravity	g	10 m s ⁻²	$\frac{2}{5} \times (a/a_{\oplus})$	$\frac{5}{2} \times (a/a_{\oplus})$
Specific heat capacity ^a	c_p	J kg ⁻¹ K ⁻¹	820	14518
Specific gas constant ^a	R	J kg ⁻¹ K ⁻¹	189	4158
Surface pressure	p_s	bar	10^{-2}	10
Longwave optical thickness at 1 bar	$\tau_{LW,1bar}$	-	0.1	100
Surface drag coefficient	C_D , via k_{vk}	-	$\times 0.1$	$\times 10$

^aMinimum values correspond to CO₂, maximum values correspond to H₂.

Table 1. Parameter bounds for our simulations. The shortwave optical thickness is set to zero, $\tau_{SW} = 0$. C_D is not a fixed parameter, so we vary the von Karman constant k_{vk} to increase and decrease C_D by an order of magnitude (Appendix A). We vary R and c_p , but require that R/c_p stays within the range of diatomic and triatomic gases ($0.23 \leq R/c_p \leq 0.29$).

signatures via transit spectroscopy. Finally, we discuss and summarize our results in Sections 9 and 10. Appendix A contains a derivation of the characteristic drag timescale for tidally locked rocky planets, Appendix B explains how we compute the wind speed scaling proposed by Wordsworth (2015), Appendix C describes how we solve the RCS model, and Appendix D lists the atmospheric equations of motion and radiative transfer for reference.

2. METHODS

We compare our models with a large number of GCM simulations. We use the FMS GCM with two-band grey gas radiative transfer and dry (non-condensing) thermodynamics. FMS has been used to simulate the atmospheres of Earth (Frierson et al. 2006), Jupiter (Liu & Schneider 2011), hot Jupiters (Heng et al. 2011), tidally locked terrestrial planets (Merlis & Schneider 2010; Mills & Abbot 2013; Koll & Abbot 2015), and non-synchronously rotating terrestrial planets (Kaspi & Showman 2015). We use the same FMS configuration as Koll & Abbot (2015). The model version we use simulates the full atmospheric dynamics and semi-grey (shortwave and longwave) radiation, and we include instantaneous dry convective adjustment. Drag is parametrized using a standard Monin-Obukhov scheme which self-consistently computes the depth of the planetary boundary layer as well as turbulent diffusion of heat and momentum. The surface is represented by an idealized “slab layer”, that is a single layer with uniform temperature and fixed depth. The “slab” temperature can be interpreted as a temperature average across the surface’s thermal skin depth (Pierrehumbert 2011b). Our simulations are all tidally locked and orbits are assumed to be circular so that the stellar flux is constant in time.

Because we only consider atmospheres that are transparent to shortwave radiation ($\tau_{SW} = 0$), the incoming stellar flux and the planetary albedo are degenerate in their effect on planetary temperature. For simplicity we set the surface albedo to zero in all our simulations and vary the incoming stellar flux. To specify the relation between longwave optical thickness and pressure, we use a standard power law of the form

$$\frac{\tau}{\tau_{LW}} = \left(\frac{p}{p_s}\right)^n. \quad (6)$$

The exponent n specifies how the optical thickness τ increases with pressure. For example, $n = 1$ if the opacity of a gas mixture is independent of pressure, and $n = 2$ if the opacity increases due to pressure broadening (Pierrehumbert 2011b; Robinson & Catling 2012). Our GCM results assume $n = 2$ or $n = 1$. The longwave optical thickness τ_{LW} is set independently of the atmosphere’s bulk composition. To constrain τ_{LW} we note that more complex radiative transfer calculations tend to find values of τ_{LW} between ~ 1 and ~ 10 at ~ 1 bar across a wide range of atmospheres, (Robinson & Catling 2014; Wordsworth 2015). We extend these bounds by one order of magnitude in each direction and require that the optical thickness at 1 bar satisfy $0.1 \leq \tau_{LW,1bar} \leq 100$. The parameter bounds for our simulations are summarized in Table 1.

Figure 1a shows the temperature structure of a representative, slowly rotating and relatively cool, GCM simulation. The planet is Earth-sized ($a = a_{\oplus}$), temperate ($T_{eq} = 283\text{K}$), has an orbital period and rotation rate of 50 days, has a moderately thick N₂-dominated atmosphere ($p_s = 1$ bar), and a longwave optical depth of unity ($\tau_{LW} = 1$). The GCM does not explicitly model a host star, but the orbital period and equilibrium temperature correspond

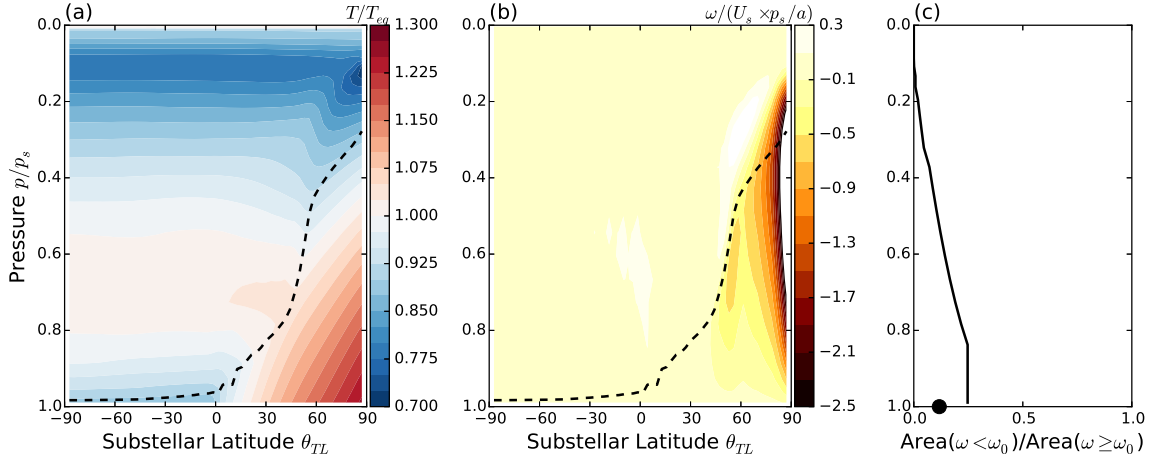


Figure 1. Temperature and circulation structure of a representative slowly rotating and weakly forced GCM simulation with $(a^2/L_{Ro}^2, t_{wave}/t_{rad}) = (0.12, 5 \times 10^{-3})$. (a) Temperature as a function of substellar latitude ($=0^\circ$ at the terminator, $=90^\circ$ at the substellar point). (b) Vertical velocity in pressure coordinates as a function of substellar latitude. (c) Area fraction of rising motion, where the dot shows the vertically averaged area fraction. The dashed black line in (a,b) shows the top of the GCM’s boundary layer. Inside the boundary layer temperature increases towards the substellar point, and air rises; outside the boundary layer temperature contours are flat and air sinks. The region of rapidly rising motions, $\omega < 0.01 \times \min(\omega)$, is narrowly focused on the substellar point while most of the atmosphere experiences weak subsidence, $\omega \gtrsim 0$. We normalize temperature by the equilibrium temperature T_{eq} , and pressure velocity by the characteristic surface speed from the heat engine $U_s \times p_s/a$ (Section 4). The planet’s physical parameters are $T_{eq} = 283\text{K}$, $a = a_\oplus$, $\Omega = 2\pi/(50\text{d})$, $p_s = 1\text{bar}$, $\tau_{LW} = 1$, and $(R, c_p) = (R, c_p)_{N_2}$.

to an early M-dwarf (M0 or M1; [Kaltenegger & Traub 2009](#), Table 1). In terms of nondimensional parameters, $(R/c_p, a^2/L_{Ro}^2, t_{wave}/t_{rad}, \tau_{LW}, t_{wave}/t_{drag}) = (2/7, 0.12, 5 \times 10^{-3}, 1, 1.4)$. Because the temperature structure is approximately symmetric about the substellar point we present this simulation in terms of a substellar latitude, i.e., the angle between substellar and antistellar point (also see [Koll & Abbot 2015](#), Appendix B). The temperature structure in Figure 1a is comparable to that found by previous studies, and temperature contours are horizontally flat outside the dayside boundary layer (dashed black line). The flat temperature contours are characteristic of the weak-temperature-gradient (WTG) regime. However, WTG does not hold on large parts of the dayside where the absorbed stellar flux creates a region of strong convection and turbulent drag, which damps atmospheric waves and allows the atmosphere to sustain horizontal temperature gradients ([Showman et al. 2013](#)). As noted by [Wordsworth \(2015\)](#), this boundary layer will be of critical importance for understanding the atmospheric circulation of rocky planets.

3. A TWO-COLUMN RADIATIVE-CONVECTIVE MODEL

In this section we present a two-column model for tidally locked planets. We divide the planet into two (dayside and nightside) vertical columns, as shown in Figure 2. The dayside is heated by stellar radiation, which triggers convection and sets an adiabatic vertical temperature profile. We assume the convective heat flux is large so that the temperature jump between dayside surface and lowest atmospheric level is small. We also assume convection is deep and do not include a stratosphere (i.e., a purely radiative layer in the upper atmosphere), so that the dayside column temperature profile in terms of optical thickness τ can be written as

$$T = T_d \left(\frac{\tau}{\tau_{LW}} \right)^\beta, \quad (7)$$

where T_d is the dayside surface temperature, τ_{LW} is the total optical thickness in the longwave, and $\beta \equiv R/(c_p n)$ is the adiabatic lapse rate in optical thickness coordinates. Next, we assume the weak-temperature-gradient (WTG) regime holds globally (i.e., also inside the dayside boundary layer). The atmosphere is therefore horizontally homogeneous and the nightside temperature structure is also described by Equation 7. Under these assumptions the entire atmosphere is in radiative-convective equilibrium, with convection governed by the dayside surface temperature T_d . The nightside surface will generally be colder than the overlying air, which leads to stable stratification and suppresses turbulent fluxes between the nightside surface and atmosphere. We idealize this situation by assuming that the nightside surface is in radiative equilibrium with the overlying atmosphere (see Fig. 2).

For a grey atmosphere on a dry adiabat, the top-of-atmosphere (TOA) upward longwave and surface downward

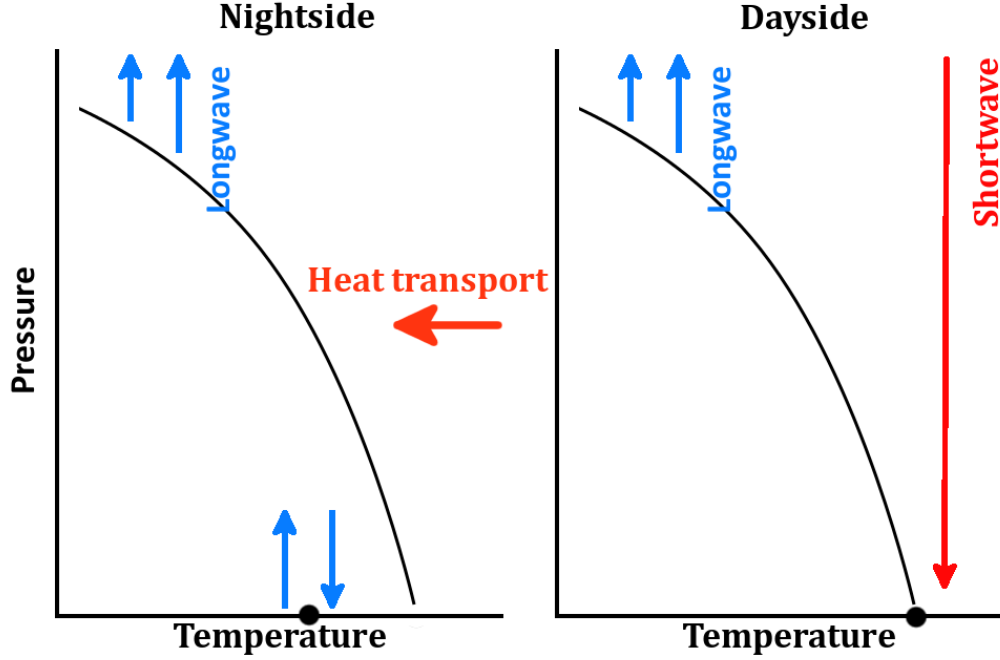


Figure 2. The two-column radiative-convective model. We assume convection on the dayside sets up an adiabatic temperature profile. Horizontal heat transport is assumed to be effective so that the atmosphere is horizontally uniform. The black dots indicate surface temperatures. The dayside surface and atmosphere are closely coupled via convection, whereas the nightside surface is in radiative equilibrium with, and generally colder than, the overlying atmosphere.

longwave fluxes are (Pierrehumbert 2011b; Robinson & Catling 2012)

$$F^\uparrow(\tau = 0) = \sigma T_d^4 e^{-\tau_{LW}} + \sigma T_d^4 \int_0^{\tau_{LW}} \left(\frac{\tau'}{\tau_{LW}} \right)^{4\beta} e^{-\tau'} d\tau', \quad (8a)$$

$$F^\downarrow(\tau = \tau_{LW}) = \sigma T_d^4 \int_0^{\tau_{LW}} \left(\frac{\tau'}{\tau_{LW}} \right)^{4\beta} e^{-(\tau' - \tau_{LW})} d\tau'. \quad (8b)$$

Using these expressions we write the dayside TOA, nightside TOA, and nightside surface energy budgets³ as

$$\frac{L_*(1 - \alpha_p)}{2} = \sigma T_d^4 e^{-\tau_{LW}} + \sigma T_d^4 \int_0^{\tau_{LW}} \left(\frac{\tau'}{\tau_{LW}} \right)^{4\beta} e^{-\tau'} d\tau' + HT, \quad (9a)$$

$$HT = \sigma T_n^4 e^{-\tau_{LW}} + \sigma T_d^4 \int_0^{\tau_{LW}} \left(\frac{\tau'}{\tau_{LW}} \right)^{4\beta} e^{-\tau'} d\tau', \quad (9b)$$

$$0 = \sigma T_n^4 - \sigma T_d^4 \int_0^{\tau_{LW}} \left(\frac{\tau'}{\tau_{LW}} \right)^{4\beta} e^{-(\tau_{LW} - \tau')} d\tau', \quad (9c)$$

where T_d is the dayside temperature, T_n is the nightside temperature, and HT is the day-night heat transport. We express the stellar flux in terms of the equilibrium temperature, $L_*(1 - \alpha_p)/2 = 2\sigma T_{eq}^4$. Next, we combine the TOA

³ We implicitly use the dayside surface energy budget by assuming that the surface-air temperature jump is negligible on the dayside.

equations to eliminate HT and use the nightside surface budget to write T_n in terms of T_d . We find

$$\sigma T_d^4 = \frac{2\sigma T_{eq}^4}{2 \int_0^{\tau_{LW}} \left(\frac{\tau'}{\tau_{LW}}\right)^{4\beta} e^{-\tau'} d\tau' + e^{-\tau_{LW}} \left[1 + \int_0^{\tau_{LW}} \left(\frac{\tau'}{\tau_{LW}}\right)^{4\beta} e^{-(\tau_{LW}-\tau')} d\tau'\right]}, \quad (10a)$$

$$\sigma T_n^4 = \frac{2\sigma T_{eq}^4 \times \int_0^{\tau_{LW}} \left(\frac{\tau'}{\tau_{LW}}\right)^{4\beta} e^{-(\tau_{LW}-\tau')} d\tau'}{2 \int_0^{\tau_{LW}} \left(\frac{\tau'}{\tau_{LW}}\right)^{4\beta} e^{-\tau'} d\tau' + e^{-\tau_{LW}} \left[1 + \int_0^{\tau_{LW}} \left(\frac{\tau'}{\tau_{LW}}\right)^{4\beta} e^{-(\tau_{LW}-\tau')} d\tau'\right]}. \quad (10b)$$

The first term in the denominator is the atmosphere's contribution to the TOA flux, the second term is the TOA flux contribution from the dayside and nightside surfaces. In practice we evaluate the definite integrals in these expressions numerically, but they can also be expressed in terms of gamma functions (Robinson & Catling 2012).

In the optically thick limit, these expressions reduce to the result of Pierrehumbert (2011b). For $\tau_{LW} \gg 1$ the exponential terms $e^{-\tau_{LW}}$ become negligibly small. The integrand in the upward flux decays exponentially at large τ' , which means we can approximate the upper limit as infinity and replace the integral with a gamma function, $\tau_{LW}^{-4\beta} \int_0^{\tau_{LW}} \tau'^{4\beta} e^{-\tau'} d\tau' \approx \tau_{LW}^{-4\beta} \int_0^{\infty} \tau'^{4\beta} e^{-\tau'} d\tau' = \tau_{LW}^{-4\beta} \Gamma(1+4\beta)$. Similarly, in the optically thick limit the downward flux at the surface has to approach unity, $\int_0^{\tau_{LW}} (\tau'/\tau_{LW})^{4\beta} e^{-(\tau_{LW}-\tau')} d\tau' \approx 1$. Combining these approximations we find $T_n \approx T_d \approx T_{eq} \tau_{LW}^{\beta} \Gamma(1+4\beta)^{-1/4}$, which is the same as Pierrehumbert's result (Equation 1). The dayside and nightside temperatures become equal in this limit because the atmosphere's downward longwave emission becomes large enough to eliminate the temperature difference between the nightside surface and the air directly above it (which in turn is equal to the dayside surface temperature).

In the optically thin limit, our model differs slightly from the result of Wordsworth (2015). For $\tau_{LW} \ll 1$ we can approximate all exponentials using Taylor series, $e^{-\tau_{LW}} = 1 + \mathcal{O}(\tau_{LW})$. Retaining only the lowest order in τ_{LW} , we write the integrals in the upward and downward fluxes both as $\tau_{LW}^{-4\beta} \int_0^{\tau_{LW}} \tau'^{4\beta} e^{\pm\tau'} d\tau' \approx \tau_{LW}^{-4\beta} \int_0^{\tau_{LW}} \tau'^{4\beta} d\tau' = \tau_{LW}/(1+4\beta)$. The atmosphere's TOA upward and surface downward emission therefore become equal, which is a well-known property of grey radiation in the optically thin limit (Pierrehumbert 2011b). Again discarding higher-order terms in τ_{LW} , we find $T_d \approx 2^{1/4} T_{eq} \times [1 - 3\tau_{LW}/(4(1+4\beta))]$ and $T_n \approx 2^{1/4} T_{eq} \tau_{LW}^{1/4} \times (1+4\beta)^{-1/4}$. This nightside temperature has the same asymptotic limit but is slightly warmer than Equation 2 from Wordsworth (2015). That is because we assume the atmosphere remains fixed to an adiabat, whereas Wordsworth (2015) assumes an atmosphere that is vertically isothermal. We will use our radiative-convective-subsiding model (Sections 5-6) to show that Wordsworth's result is a limiting expression for atmospheres that are very hot or thin, $t_{wave}/t_{rad} \gtrsim 1$, whereas our results in this Section apply for atmospheres that are cold or thick, $t_{wave}/t_{rad} \lesssim 10^{-4}$. Nevertheless, β is always of order unity so the difference between Equation 2 and our result is small in the optically thin regime.

Next, we compare the previous scalings and our radiative-convective (RC) model with our GCM simulations. Figure 3 shows dayside (top) and nightside (bottom) average surface temperatures of many simulations. To represent all GCM results in a single figure, we normalize surface temperatures using the equilibrium temperature T_{eq} of each simulation. We only show simulations with $\beta = 1/7$, i.e., $(R, c_p, n) = (R_{N_2}, c_{p,N_2}, 2)$. First, as we showed above, the RC model tends towards the expressions of Pierrehumbert and Wordsworth in the optically thick and thin regimes (compare solid line with dashed and dotted lines). While the two approximate expressions diverge at $\tau_{LW} = 1$, our model provides a smooth fit in this region. Second, the RC model captures dayside surface temperatures very well, with deviations between the RC model and the GCM simulations smaller than $0.1 \times T_{eq}$. The RC model systematically overpredicts dayside temperatures because of its idealized geometry, which represents the entire dayside as a single column. For example, the dayside-average temperature of an airless planet in pure radiative equilibrium is $4\sqrt{2}/5 \times T_{eq} \approx 1.13T_{eq}$, whereas the RC model predicts $2^{1/4} \times T_{eq} \approx 1.19T_{eq}$. Third, the RC model captures the general trend of nightside surface temperature with τ_{LW} . However, Figure 3 also shows that nightside temperatures exhibit a much wider spread than dayside temperatures, which is not captured by the RC model.

There are two reasons for the spread in nightside temperatures: first, rapidly rotating atmospheres develop horizontally inhomogeneous nightsides, and second, tidally locked atmospheres do not have an adiabatic temperature structure on the nightside. We address rotation in Section 7, here we consider the effect of temperature structure. Figure 4a shows the vertical temperature structure of a slowly rotating simulation. The grey lines show the vertical temperature profiles at each horizontal GCM grid point, which form a wide envelope. The hottest temperatures at the right side of the envelope correspond to the substellar point. These profiles are indeed adiabatic, which can be seen from the fact that they are parallel to the temperature profile of the RC model (dashed red-blue line). However,

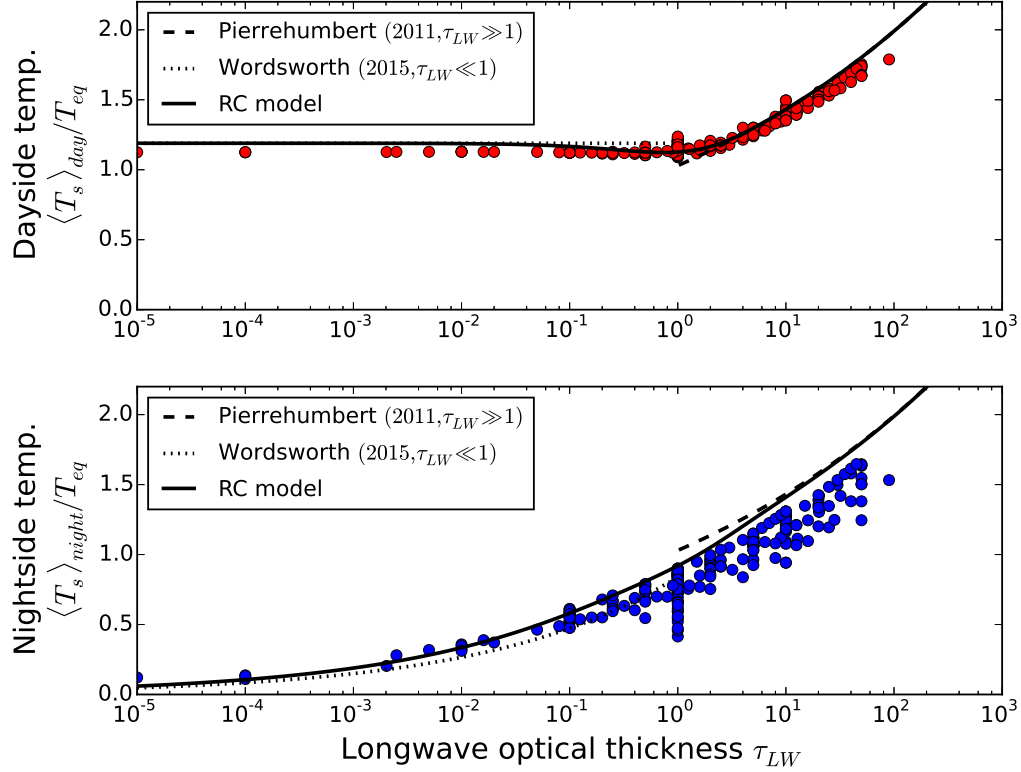


Figure 3. Our radiative-convective (RC) model captures the basic dependency of surface temperature on τ_{LW} and joins previous asymptotic limits. Top: Average dayside surface temperatures of many GCM simulations ($N = 251$). Bottom: Average nightside surface temperatures. Dashed and dotted curves show previously-derived asymptotic scalings in the optically thick ($\tau_{LW} \gg 1$, Pierrehumbert 2011b) and optically thin limits ($\tau_{LW} \ll 1$, Wordsworth 2015). The solid curve shows the RC model (Section 3). While the RC model closely matches the GCM dayside temperatures, it does not account for the wide spread in nightside temperatures. All shown simulations use $n = 2$ and $(R, c_p) = (R, c_p)_{N_2}$.

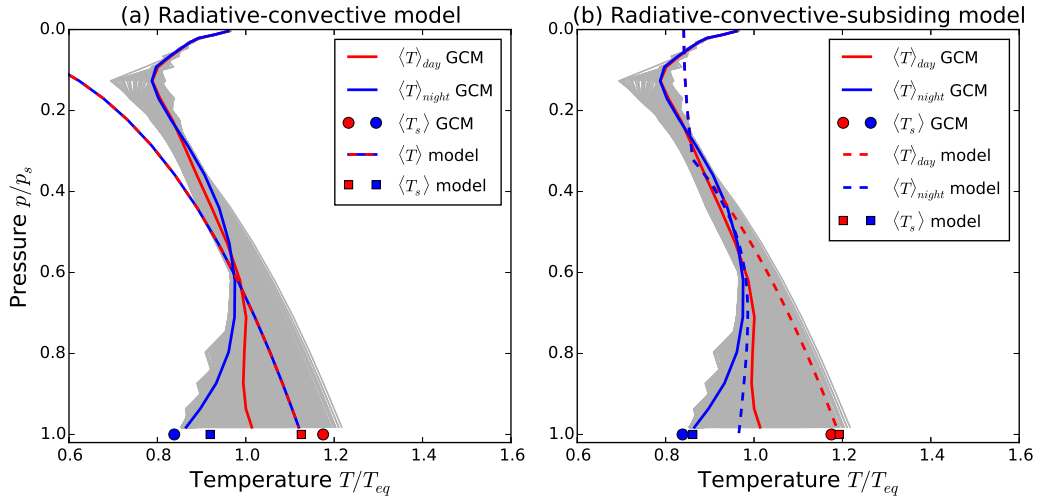


Figure 4. Temperature structure of a slowly rotating GCM simulation ($a^2/L_{Ro}^2 = 0.1$), compared with the radiative-convective (RC, left) and the radiative-convective-subsiding model (RCS, right). Solid curves correspond to dayside (red) and nightside-averaged (blue) GCM temperature profiles, and GCM temperature profiles at each latitude and longitude (grey). Left: Although the RC model (mixed red-blue curve) qualitatively captures the temperature structure, it does not capture the nightside inversion and thus overpredicts the nightside surface temperature (compare blue square with blue circle). Right: the RCS model (dashed curves) accounts for imperfect day-night heat transport and qualitatively captures the nightside inversion structure. This leads to a better fit of nightside surface temperature than for the RC model. The planet's physical parameters are $T_{eq} = 400\text{K}$, $a = a_{\oplus}$, $\Omega = 2\pi/(50\text{d})$, $p_s = 0.5\text{bar}$, $\tau_{LW} = 1$, $(R, c_p) = (R, c_p)_{N_2}$, and $g = 5\text{m s}^{-2}$.

as the dayside and nightside averaged profiles show, large parts of the atmosphere do *not* follow an adiabat (solid red and blue lines in Fig. 4a). The deviation arises because WTG breaks down inside the dayside boundary layer (Fig. 1a). This allows the atmosphere outside the boundary layer to decouple from regions of convection, and develop a strongly non-adiabatic temperature profile. In particular, Figure 4 shows that the nightside average (blue line) forms a strong inversion below $p/p_s \sim 0.6$, which means the nightside is stably stratified and far from radiative-convective equilibrium. Nightside inversions are a robust feature of tidally locked atmospheres and have been found in a range of simulations (e.g., Joshi et al. 1997; Merlis & Schneider 2010; Leconte et al. 2013), but are not captured by the RC model. As a consequence the RC model produces a warmer nightside atmosphere and therefore also a warmer nightside surface than the GCM (compare blue square and blue circle in Fig. 4a). We present a model that captures the nightside temperature structure in Section 5. However, to do so we have to account for atmospheric dynamics, which show up via the parameters t_{wave}/t_{rad} and t_{wave}/t_{drag} . To address the dynamics we first have to develop a theory of large-scale wind speeds and the atmospheric circulation, which we turn to in the next section.

4. A HEAT ENGINE SCALING FOR WIND SPEEDS

Earth’s atmosphere acts as a heat engine: it absorbs heat near the surface at a high temperature and emits heat to space at a low temperature, which allows the atmosphere to do work and balance frictional dissipation (Peixoto & Oort 1984). On Earth the heat engine framework has been used to derive upper bounds on the strength of tropical moist convection (Renno & Ingersoll 1996; Emanuel & Bister 1996) and small-scale circulations such as hurricanes (Emanuel 1986).

In this section we idealize the atmospheric circulation of a tidally locked planet as a single overturning cell between the substellar and antistellar point. We model the circulation as an ideal heat engine to place an upper bound on its circulation strength. The ideal heat engine is an upper bound because additional physical processes, such as diffusion, lead to irreversible production of entropy and decrease the efficiency of a heat engine below its ideal limit (Pauluis & Held 2002). As shown in Figure 5, the atmosphere absorbs heat near the dayside surface at a hot temperature

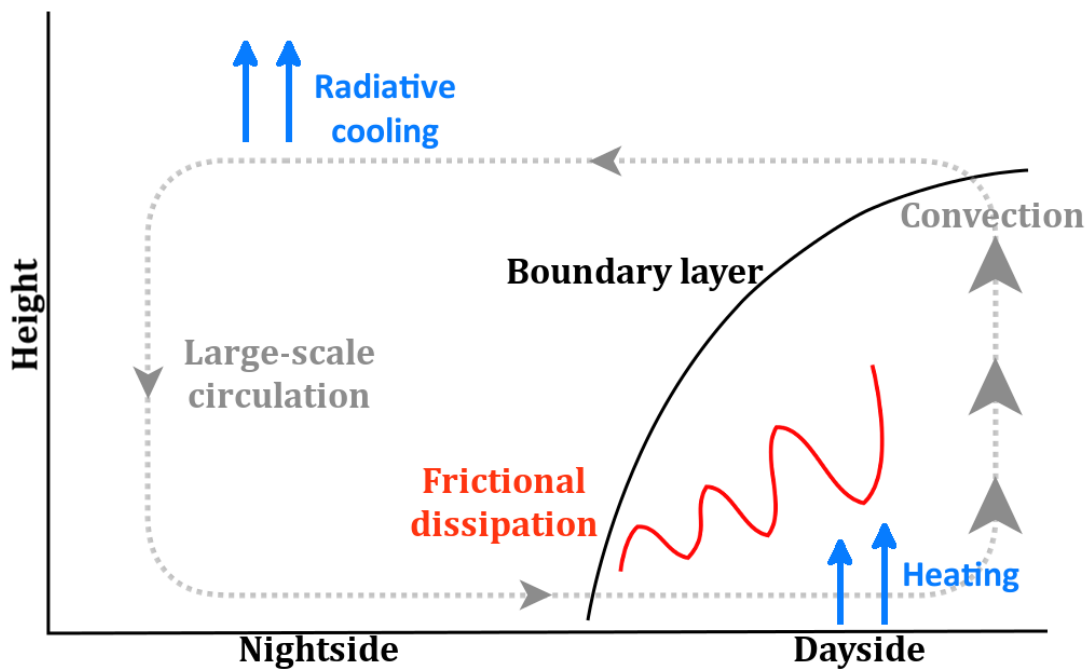


Figure 5. A diagram of the atmospheric heat engine. The heat engine is driven by dayside heating and cooling to space. Frictional dissipation in the dayside boundary layer limits the strength of the resulting day-night atmospheric circulation.

and emits it to space at a cold temperature. These temperatures are defined in terms of entropy-weighted averages over which the atmosphere absorbs and gives off heat (Emanuel & Rotunno 1989; Pauluis & Held 2002). Here we idealize the dayside as a single column that follows an adiabat. Entropy is therefore vertically constant on the dayside, which means the temperature at which the atmosphere absorbs heat is equal to the dayside surface temperature, T_d . We approximate the cold temperature as the planet’s effective emission temperature to space, i.e., its equilibrium temperature T_{eq} . The parcel does work against friction in the boundary layer which is given by $W = C_D \rho_s U_s^3$ (Bister & Emanuel 1998). Here W is the work, ρ_s is the surface density, and U_s is a surface wind speed, which we take to be the dayside-average surface wind (Fig. 5). Using Carnot’s theorem,

$$W = \eta Q_{in}, \quad (11)$$

where $\eta = (T_d - T_{eq})/T_d$ is the atmosphere’s thermodynamic efficiency, and $Q_{in} = 2\sigma T_{eq}^4 \times (1 - e^{-\tau_{LW}})$ is the amount of energy that is available to drive atmospheric motion. We note that the dayside-averaged incoming stellar flux is equal to $2\sigma T_{eq}^4$, but we additionally account for the fact that only a fraction $1 - e^{-\tau_{LW}}$ of stellar energy is available to the atmosphere, while the remainder is immediately re-radiated from the surface to space.

We find the following upper bound on the dayside average surface wind speed,

$$\begin{aligned} U_s &= \left[\frac{T_d - T_{eq}}{T_d} \times (1 - e^{-\tau_{LW}}) \frac{2\sigma T_{eq}^4}{C_D \rho_s} \right]^{1/3} \\ &= \left[\frac{T_d - T_{eq}}{T_d} \times (1 - e^{-\tau_{LW}}) \frac{2RT_d \sigma T_{eq}^4}{C_D p_s} \right]^{1/3} \\ &= \left[(T_d - T_{eq}) \times (1 - e^{-\tau_{LW}}) \frac{2R\sigma T_{eq}^4}{C_D p_s} \right]^{1/3}, \end{aligned} \quad (12)$$

where we used the ideal gas law to substitute for ρ_s in the second step. The only unknown in this equation is the dayside surface temperature T_d . As we saw in Section 3, T_d was already well constrained by the radiative-convective model (Fig. 3). In this section we therefore close the model using T_d from Equation 10a (but note that we will self-consistently solve for T_d in Section 5).

Figure 6 compares dayside averaged surface wind speeds $\langle U_s \rangle$ with a numerical wind speed scaling from Wordsworth (2015, see Appendix B) and our analytical heat engine scaling. We note that Wordsworth considered the optically thin limit, whereas our results are valid for arbitrary τ_{LW} . Wordsworth derived a scaling by assuming weak temperature gradients hold globally. In a weak-temperature-gradient (WTG) atmosphere, radiative cooling leads to subsidence, which Wordsworth assumed in turn drives the large-scale circulation. Figure 6 shows that the GCM wind speeds span two orders of magnitude, from 3 m s^{-1} up to about 300 m s^{-1} . The Wordsworth (2015) scaling seems to match these wind speeds at $\mathcal{O}(1) \text{ m s}^{-1}$. However, it predicts a strong decrease, down to less than 10^{-2} m s^{-1} , which is several orders of magnitude smaller than the GCM results (Fig. 6a). The mismatch arises because Wordsworth’s global WTG scaling assumes winds are purely driven by radiative cooling, $U_s \propto \tau_{LW}$ (Appendix B), so U_s should rapidly vanish in the optically thin limit. Instead, Figure 1 shows that WTG balance breaks down in regions that are strongly convecting. The convecting regions in turn govern the return flow from the nightside to the dayside, which means that the effect of friction on the large-scale circulation cannot be neglected. Our heat engine scaling includes this effect and predicts very different dynamics. For example, in the optically thin limit the dayside temperature is approximately constant and $1 - e^{-\tau_{LW}} \approx \tau_{LW}$, so $U_s \propto \tau_{LW}^{1/3}$ (Equation 12). Figure 6b supports our theory. The slope predicted by the heat engine provides an excellent fit to the GCM results. Moreover, we expect the heat engine to provide an upper bound on surface wind speeds. Our expectation is confirmed by the GCM simulations, which fall below the dashed black line in Figure 6b. In addition, the overestimate of $\langle U_s \rangle$ is small and generally amounts to less than a factor of 4 (grey dashed line in Figure 6b), with most simulations falling about a factor of 2 below the ideal limit.

Next, we use the surface wind speed scaling to place an upper bound on the strength of the day-night circulation. Of particular interest to us is the large-scale vertical motion on the nightside, which we will show governs the day-night heat transport and is critically important for the temperature structure on the nightside (Section 5). We express all vertical motions using pressure coordinates, that is, using the pressure velocity $\omega \equiv Dp/Dt$ where $\omega > 0$ means sinking motions. We take the surface wind speed U_s to be the characteristic horizontal velocity within the boundary layer. We relate the horizontal velocity in the boundary layer to the pressure velocity near the substellar point using mass

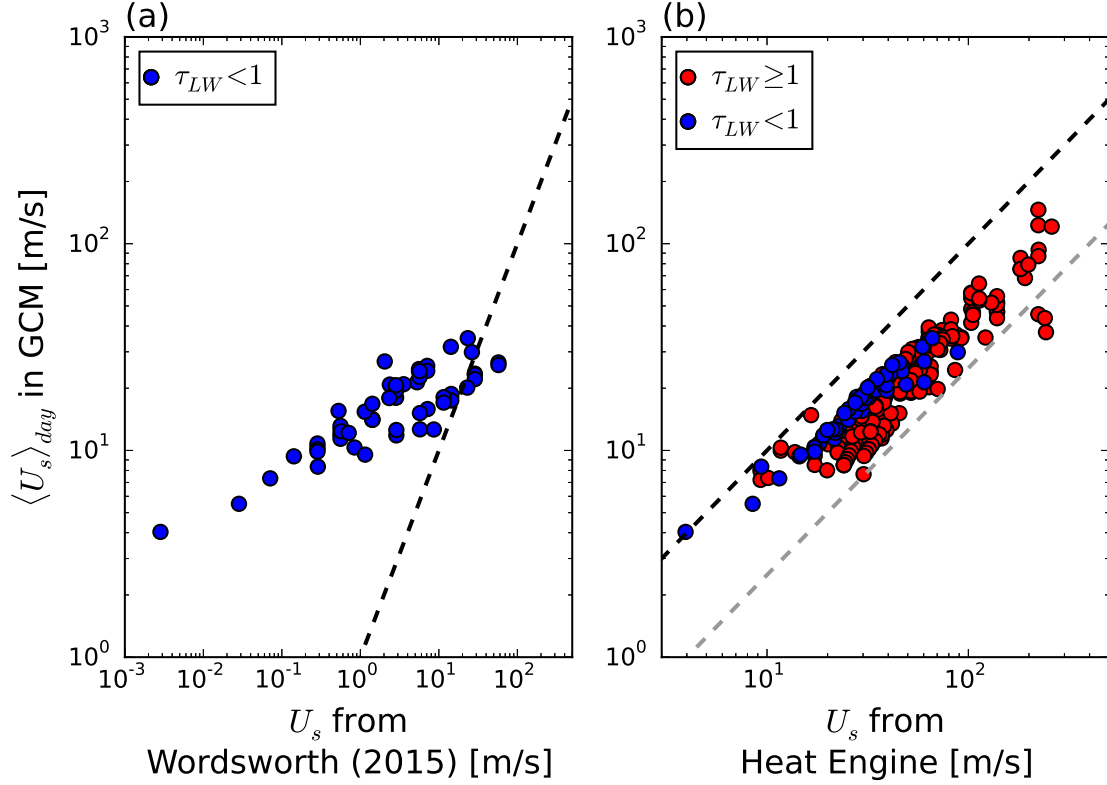


Figure 6. Two different surface wind speed scalings compared with many GCM results ($N = 271$). Left: scaling for dayside surface wind speed from [Wordsworth \(2015\)](#), which was derived assuming optically thin atmospheres ($\tau_{LW} < 1$). Right: our scaling for average surface wind speed for an ideal heat engine (Eqns. 12 and 10a). The GCM simulations are less efficient than ideal heat engines and therefore have smaller surface wind speeds. The grey dashed line corresponds to an inefficiency factor of $1/4$.

conservation (Equation D14),

$$\frac{\omega_{up}}{p_s} \sim \frac{U_s}{a}. \quad (13)$$

Figure 1b supports this scaling, and ω/ω_{up} near the substellar point is of order unity. However, Figure 1b also shows that there is a large asymmetry between rising and sinking motions. While air rises rapidly near the region of strongest convection at the substellar point, it sinks slowly over a large area outside the boundary layer. Figure 1c quantifies the asymmetry using A_{up}/A_{down} , the fraction of the atmosphere in which air rises versus sinks⁴. In the shown simulation rising air never covers more than 20% of the atmosphere, while its vertically averaged value is about 10% (dot in Fig. 1c). The asymmetry in vertical motions arises from the geometric asymmetry of the incoming stellar flux, and is distinct from the asymmetry of rising and sinking motions in Earth’s tropics which is caused by the condensation of water during convection. Because upward and downward mass fluxes have to balance across a horizontal slice of atmosphere,

$$\rho A_{up} \omega_{up} = \rho A_{down} \omega_{down}, \quad (14)$$

where ρ is the density of an air parcel, we can relate the pressure velocity on the nightside to the dayside surface wind,

$$\omega_{down} = \frac{A_{up}}{A_{down}} \frac{p_s}{a} \times U_s. \quad (15)$$

Equation 15 explains how tidally locked planets sustain weak downward motions despite very large horizontal wind speeds. The time for a parcel of air to be advected horizontally is $t_{adv} = a/U_s$ whereas the time for a parcel to subside (that is, be advected vertically) is $t_{sub} = p_s/\omega_{down} = A_{down}/A_{up} \times t_{adv}$. For $A_{down}/A_{up} \sim 10$ it takes a parcel of air

⁴ Because the uppermost layers of the atmosphere show both weakly rising and falling motions we define A_{up} as the area with “significant” upward motion where $\omega \leq 0.01 \times \min(\omega)$.

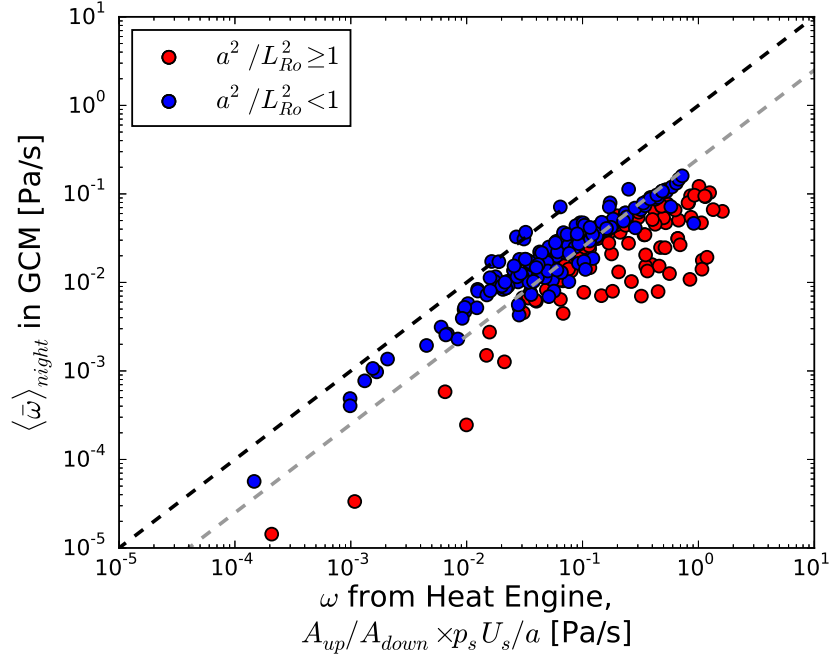


Figure 7. The heat engine scaling provides a strong constraint on the day-night atmospheric circulation. Shown is the vertical velocity in pressure coordinates predicted by the heat engine scaling (x-axis), compared with the average nightside pressure velocity in the GCM (y-axis). Rapidly rotating atmospheres, $a^2/L_{Ro}^2 \geq 1$, develop inhomogeneous nightsides and can locally sustain smaller pressure velocities (Section 7).

ten times longer to sink back to the surface on the nightside than to be advected from the nightside to the dayside. The same comparison also explains why day-night temperature gradients of tidally locked planets are not set by the advective timescale and instead depend on the ratio of subsidence and radiative timescales (Section 6).

Next, Figure 7 compares the pressure velocity ω_{down} from Equation 15 with the mass-weighted vertically and horizontally averaged pressure velocities, $\langle \bar{\omega} \rangle_{night}$, from GCM simulations. In the comparison we use Equation 12 to predict U_s but still diagnose A_{up}/A_{down} directly from GCM output. First, because the heat engine provides an upper limit on U_s it also provides an upper limit on ω_{down} . The GCM simulations indeed fall almost entirely below the dashed black line in Figure 6b. We note that in deriving Equation 12 we neglected some factors that we expect to be small (e.g., geometric factors), but which explain why some GCM simulations slightly exceed the value predicted by the scaling. Second, we find that relatively slowly rotating atmospheres (blue dots) closely follow the heat engine scaling and most of them deviate less than a factor of 4 from it (grey dashed line). Third, rapidly rotating atmospheres (red dots) still follow the scaling qualitatively but $\langle \bar{\omega} \rangle_{night}$ is smaller than in slowly rotating atmospheres. The larger deviation arises because rapidly rotating atmospheres develop inhomogeneous nightsides (Section 7). In the extratropics the flow then becomes geostrophic which in turn suppresses vertical motions by $\mathcal{O}(Ro) \ll 1$, where Ro is the Rossby number (Showman et al. 2010).

We conclude that atmospheres of dry tidally locked planets are dominated by dayside boundary layer friction. The heat engine framework successfully constrains the amount of dissipation and surface wind speeds within the boundary layer. Combined with the areal asymmetry between rising and sinking motions, we find an upper bound on the nightside vertical velocity. Our result is distinct from previous scalings that have been proposed for exoplanets. We will use our result in the next section to constrain the thermal structure of the nightside.

5. A TWO-COLUMN RADIATIVE-CONVECTIVE-SUBSIDING MODEL

As we showed in Figures 3 and 4, to understand nightside surface temperatures of tidally locked planets we need to account for an imperfect day-night heat transport and to better constrain the nightside atmospheric temperature structure. In this section we develop a two-column model that does so. We again divide the atmosphere into two dayside and nightside columns, shown in Figure 8. As in Section 3 the dayside column is strongly convecting, but we allow the nightside temperature profile to deviate from an adiabat. Both columns are capped by a stratosphere, that is, a layer in pure radiative equilibrium.

As in our radiative-convective model, convection sets an adiabatic temperature profile on the dayside. The dayside

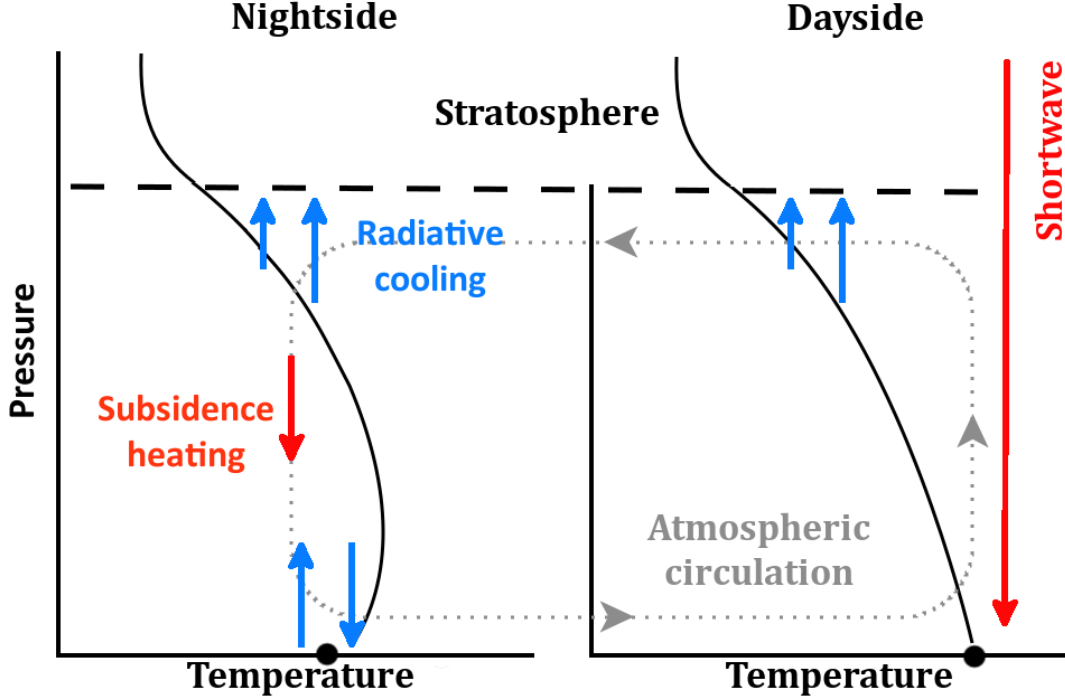


Figure 8. A diagram of the two-column radiative-convective-subsiding model. We assume convection sets an adiabatic temperature profile on the dayside, and a balance between radiative cooling and subsidence heating sets the temperature profile on the nightside. In addition, both columns are capped by a horizontally uniform and purely radiative stratosphere. The day-night circulation and the rate of subsidence are governed by the atmospheric heat engine.

temperature profile is therefore

$$T = T_d \left(\frac{\tau}{\tau_{LW}} \right)^\beta. \quad (16)$$

The nightside is in weak-temperature-gradient (WTG) balance. WTG balance follows from the thermodynamic equation (Equation D15),

$$\frac{\partial T}{\partial t} + \mathbf{u} \cdot \nabla T + \omega \frac{\partial T}{\partial p} = \frac{RT\omega}{c_p p} + \frac{g}{c_p} \frac{\partial F}{\partial p} + \frac{g}{c_p} \frac{\partial \mathcal{D}}{\partial p}, \quad (17)$$

where \mathbf{u} is the horizontal velocity, ω is the pressure velocity ($\omega > 0$ for subsiding air), F is the net radiative flux (the sum of upward and downward longwave fluxes, $F = F^\uparrow - F^\downarrow$), and \mathcal{D} is the energy flux due to diffusion. The left side of the thermodynamic equation represents advection, the first term on the right is heating/cooling due to compression/expansion as air parcels move vertically, the second term on the right is radiative heating/cooling, and the third term represents the effect of small-scale convection inside the boundary layer. In equilibrium $\partial T/\partial t = 0$, and \mathcal{D} is negligible on the nightside because the nightside is stably stratified. As long as horizontal temperature gradients are small on the nightside the thermodynamic equation then reduces to WTG balance

$$\omega \left(\frac{\partial T}{\partial p} - \frac{RT}{c_p p} \right) \approx \frac{g}{c_p} \frac{\partial F}{\partial p}. \quad (18)$$

Equation 18 entails that radiative cooling is accompanied by subsidence as follows. In a cooling layer the net radiative flux decreases towards the surface, $\partial F/\partial p < 0$. The lapse rate has to be smaller than, or equal to, the adiabatic lapse rate because the atmosphere would otherwise start convecting, $\partial T/\partial p \leq RT/(c_p p)$. It follows that $\omega > 0$.

In Earth's tropics the vertical temperature structure, $\partial T/\partial p$, and radiative fluxes, $\partial F/\partial p$, are set by small regions of moist convection, in which case WTG can be used to predict the large-scale ω (Sobel et al. 2001). In this section we

pursue the opposite approach: because ω is set by the day-night circulation which, in turn, is limited by friction in the dayside boundary layer (Section 4), we will use WTG balance to solve for T and F . For simplicity we replace ω with its vertical average $\bar{\omega}$. Because we assume that horizontal variations are small, we also replace all partial derivatives with normal derivatives. We rewrite WTG balance in optical depth coordinates and combine it with the Schwarzschild equation for the radiative flux F (Equation D16),

$$\frac{c_p \bar{\omega}}{g} \left(\frac{dT}{d\tau} - \frac{\beta T}{\tau} \right) = \frac{dF}{d\tau}, \quad (19a)$$

$$\frac{d^2 F}{d\tau^2} - F = -2 \frac{d(\sigma T^4)}{d\tau}. \quad (19b)$$

Given boundary conditions, these equations can be solved for T and F . The left side of Equation 19a represents the vertical energy flux due to subsidence (in W m^{-2}). In the WTG regime subsidence is how the atmosphere transports heat between dayside and nightside. Atmospheres with strong subsidence (large $\bar{\omega}$) will tend to have nightsides that are close to an adiabat, while atmospheres with very weak subsidence will tend to approach pure radiative equilibrium on their nightsides (i.e., $dF/d\tau \approx 0$).

To solve for T and F on the nightside we need to specify an upper boundary condition. A natural choice is the tropopause, τ_0 , up to which convection rises on the dayside. Above τ_0 the atmosphere is in pure radiative equilibrium, $dF/d\tau = 0$. We assume the stratosphere is horizontally uniform, which means it has the same temperature structure as in Pierrehumbert (2011b),

$$T_{strat} = T_{eq} \left(\frac{1 + \tau}{2} \right)^{1/4}. \quad (20)$$

We can now specify the boundary conditions for the nightside atmosphere and Equations 19. Because WTG balance is a first-order equation and the radiative equation is a second-order equation we require three conditions,

$$T(\tau_0) = T_{strat}(\tau_0), \quad (21a)$$

$$dF(\tau_0)/d\tau = 0, \quad (21b)$$

$$F(\tau_{LW}) = 0. \quad (21c)$$

The first equation is temperature continuity at the tropopause. The second is the stratospheric energy budget, that is, pure radiative equilibrium. The third condition is the nightside surface energy budget. Because the nightside surface is in radiative equilibrium with the overlying atmosphere, $F^\uparrow(\tau_{LW}) = F^\downarrow(\tau_{LW})$, the net radiative flux $F = F^\uparrow - F^\downarrow$ has to vanish at the surface. The only unknown in these boundary conditions is the tropopause height τ_0 .

The tropopause height τ_0 is in turn governed by convection on the dayside. On the dayside, the convective temperature profile (Equation 16) has to match the stratospheric temperature profile (Equation 20) at τ_0 , so

$$\begin{aligned} T_d \left(\frac{\tau_0}{\tau_{LW}} \right)^\beta &= T_{strat}(\tau_0), \\ T_d \left(\frac{\tau_0}{\tau_{LW}} \right)^\beta &= T_{eq} \left(\frac{1 + \tau_0}{2} \right)^{1/4}. \end{aligned} \quad (22)$$

Finally, we use the top-of-atmosphere (TOA) energy budget to constrain T_d . The global TOA energy budget is

$$2\sigma T_{eq}^4 = F(0)_{day} + F(0)_{night}. \quad (23)$$

The left side is the incoming solar radiation and the right side is the dayside and nightside outgoing longwave radiation (OLR). To specify these fluxes we note that the stratosphere is in radiative equilibrium, $dF/d\tau = 0$, so the OLR has to match the net flux at the tropopause, $F(0) = F(\tau_0)$. The net radiative flux at the dayside tropopause is

$$F(\tau_0)_{day} = \sigma T_d^4 e^{-(\tau_{LW} - \tau_0)} + \sigma T_d^4 \int_{\tau_0}^{\tau_{LW}} \left(\frac{\tau'}{\tau_{LW}} \right)^{4\beta} e^{-(\tau' - \tau_0)} d\tau' - \sigma T_{eq}^4 \frac{\tau_0}{2}. \quad (24)$$

The first two terms are the upwelling flux at the dayside tropopause (from the surface and atmosphere respectively), and the third term is downward flux from the stratosphere (Robinson & Catling 2012). The global TOA energy budget therefore is,

$$2\sigma T_{eq}^4 = \sigma T_d^4 e^{-(\tau_{LW} - \tau_0)} + \sigma T_d^4 \int_{\tau_0}^{\tau_{LW}} \left(\frac{\tau'}{\tau_{LW}} \right)^{4\beta} e^{-(\tau' - \tau_0)} d\tau' - \sigma T_{eq}^4 \frac{\tau_0}{2} + F(\tau_0). \quad (25)$$

Equations 21-25 determine the tropopause height τ_0 , the dayside surface temperature T_d , and the nightside OLR $F(\tau_0)$.

Finally, we constrain the pressure velocity $\bar{\omega}$ on the nightside. We showed in Figure 7 that the heat engine scaling allows us to place an upper bound on $\bar{\omega}$ once we account for the fact that atmospheres are imperfect heat engines and once we know the relative fraction of rising versus subsiding motions, A_{up}/A_{down} (we consider rotation in Section 7). In this section we incorporate these effects via

$$\omega_{down} = \chi \times \frac{p_s U_s}{a} \quad (26)$$

where χ captures the inefficiency of the heat engine as well as the smallness of A_{up}/A_{down} . We again use Equation 12 to compute U_s , but now we self-consistently solve for the dayside temperature T_d . To constrain χ we note that the asymmetry between rising and sinking motions is set by the tidally locked geometry and hence should not vary much between different simulations. We use $A_{up}/A_{down} \approx 0.1$ from Figure 1c as a representative value. Similarly, for slowly rotating atmospheres we found that $\bar{\omega}$ falls between the value predicted by the heat engine and about a factor of four less (Fig. 7), so we choose a representative inefficiency of 1/2. Combining these two, we find $\chi = 1/20$. Because rapidly rotating atmospheres tend to have weaker nightside subsidence (Figure 7), our choice of χ is an upper bound for ω_{down} and will overestimate the day-night heat transport on rapidly rotating planets. We emphasize that χ is the only tunable parameter in our model and is fixed to a single value. We do not change χ when we compare the radiative-convective-subsiding model with different GCM simulations.

We numerically solve the model to find the nightside temperature T and radiative flux F , the dayside surface temperature T_d , the nightside surface temperature T_n and the tropopause height τ_0 . The boundary conditions for T and F are specified at the tropopause and at the surface, so we use a shooting method (Appendix C). We note that the Schwarzschild equation (Equation 19b) becomes difficult to solve accurately in the optically thick limit because the radiative boundary conditions at the tropopause and surface decouple at large τ_{LW} (Equations 21b,c). Nevertheless, the underlying physics do not change qualitatively once $\tau_{LW} \gg 1$. We therefore avoid these issues by limiting our numerical solver to atmospheres with $\tau_{LW} \leq 15$.

Figure 4b compares the radiative-convective-subsiding (RCS) model with the same slowly rotating GCM simulation as in Figure 4a. The RCS model produces an adiabatic temperature profile on the dayside and an inversion on the nightside. Compared to the radiative-convective model (RC, Fig. 4a), the RCS model produces a colder nightside and a warmer dayside because it does not assume that the day-night heat transport is necessarily highly effective. The predicted temperatures match the GCM significantly better, particularly on the nightside. The RCS model also places the tropopause at $p/p_s \sim 0.3$, whereas the GCM tropopause is higher up, at $p/p_s \sim 0.1$. The high tropopause in the GCM arises because it is set by the deepest convection and hottest temperatures near the substellar point instead of the average dayside temperature (Fig. 4b), which the RCS model does not account for. Finally, the inversion structure in the RCS model is somewhat skewed compared with the GCM, and the inversion occurs higher up in the atmosphere (Fig. 4b). The raised inversion is likely due to our assumption of a vertically constant value of ω . Nevertheless, given the simplicity of the RCS model, we consider the fit between the RCS model and the GCM highly encouraging. We emphasize that the RCS model is obtained via a simple numerical solution, and is conceptually much simpler (and computationally much cheaper) than the full GCM.

Next, Figure 9 compares the RC and RCS models with many GCM simulations. The top row compares the radiative-convective model (RC) with the GCM, the bottom row does the same for the radiative-convective-subsiding (RCS) model. We note that in rapidly rotating atmospheres ($a^2/L_{Ro}^2 \geq 1$) WTG balance does not hold at higher latitudes, and both models should break down. However, WTG balance actually provides a good approximation of the nightside structure even at rapid rotation provided the atmosphere is not too hot or thin ($t_{wave}/t_{rad} \gtrsim 5 \times 10^{-2}$). We explain this threshold in Sections 6 and 7, here we simply mark simulations for which the RCS model could break down in red and all other simulations in blue. First, as we already explained for Figure 4b, the RCS model generally predicts warmer daysides than the RC model, which already overestimates dayside temperatures slightly (see right panels in Fig. 9). To quantify the goodness of fit between the GCM and our models, we compute r^2 values for the simulations marked in blue. For dayside temperatures we find $r^2 = 0.82$ with the RC model, and $r^2 = 0.23$ with the RCS model. These values underline that the RC model already captures the basic structure of the dayside. Improving the fit even further would require addressing the spatial inhomogeneity on the dayside (Fig. 1), whereas the reduced heat transport in the RCS model actually worsens its dayside fit. Second, as in Figure 3, Figure 9 shows that the RC model overpredicts nightside surface temperatures (top left panel). In contrast, the RCS model fits the GCM values extremely well (bottom left panel). For nightside temperatures we find $r^2 = 0.76$ with the RC model, while the RCS

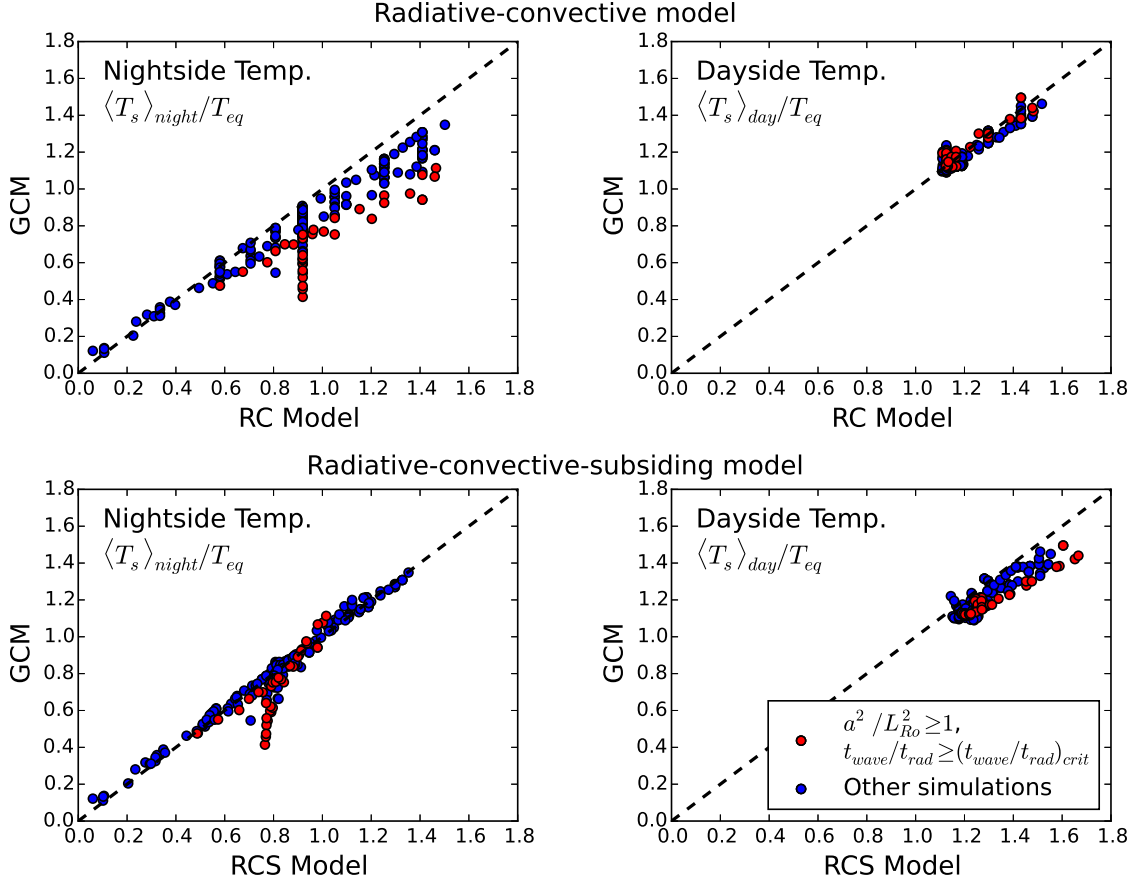


Figure 9. Comparison of surface temperatures predicted by the radiative-convective (RC) and radiative-convective-subsiding (RCS) models with many GCM simulations ($N = 241$). Red dots represent simulations that are both rapidly rotating and have hot/thin atmospheres ($a^2/L_{Ro}^2 \geq 1$ and t_{wave}/t_{rad} exceeds threshold from Equation 34), blue dots show all other simulations. Top left: average nightside temperature, RC model vs. GCM. Top right: average dayside temperature, RC model vs. GCM. Bottom left: average nightside temperature, RCS model vs. GCM. Bottom right: average dayside temperature, RCS model vs. GCM. The RCS model captures nightside temperatures much better than the RC model. The RCS model breaks down only for atmosphere that are both rapidly rotating and hot/thin (red dots; see Section 7).

model essentially reproduces the GCM results with a fit of $r^2 = 0.98$.

To conclude, we have formulated a radiative-convective-subsiding model that utilizes WTG balance combined with the heat engine scaling for the large-scale circulation to capture the day-night heat transport and nightside temperature structure. Our model captures the day-night temperature structure of many GCM simulations extremely well. We provide an intuitive understanding of the model results in the next section.

6. TRANSITION TO LARGE DAY-NIGHT TEMPERATURE GRADIENTS

In this section we explain the threshold at which atmospheres of tidally locked rocky planets develop large day-night temperature gradients. We point out again that hot Jupiter theories suggest this should occur when $t_{wave}/t_{rad} \gtrsim 1$ (Section 1). In contrast, we show that on rocky planets the threshold is up to two orders of magnitude smaller and temperature gradients become large when $t_{wave}/t_{rad} \gtrsim \mathcal{O}(10^{-2})$. The small threshold is important because it means rocky exoplanets are relatively more sensitive to the parameter t_{wave}/t_{rad} , so planets that are relatively cool or have thick atmospheres still exhibit large day-night temperature differences. Finally, we relate the RCS model back to previous theories by showing that it reduces to our RC model for $t_{wave}/t_{rad} \lesssim 10^{-4}$ and to Wordsworth (2015)'s result for $t_{wave}/t_{rad} \gtrsim 1$ and $\tau_{LW} \ll 1$.

To start, we consider the thermodynamic equation under WTG balance (Equation 19a). WTG balance expresses a balance between subsidence heating and radiative cooling, and we nondimensionalize it using $\hat{T} = T/T_{eq}$ and $\hat{F} = F/(\sigma T_{eq}^4)$. We find that the ratio of subsidence heating to radiative cooling is governed by two parameters,

$$\frac{d\hat{T}}{d\tau} - \beta \frac{\hat{T}}{\tau} = \left(\frac{t_{sub}}{t_{rad}} \right) \frac{d\hat{F}}{d\tau}, \quad (27)$$

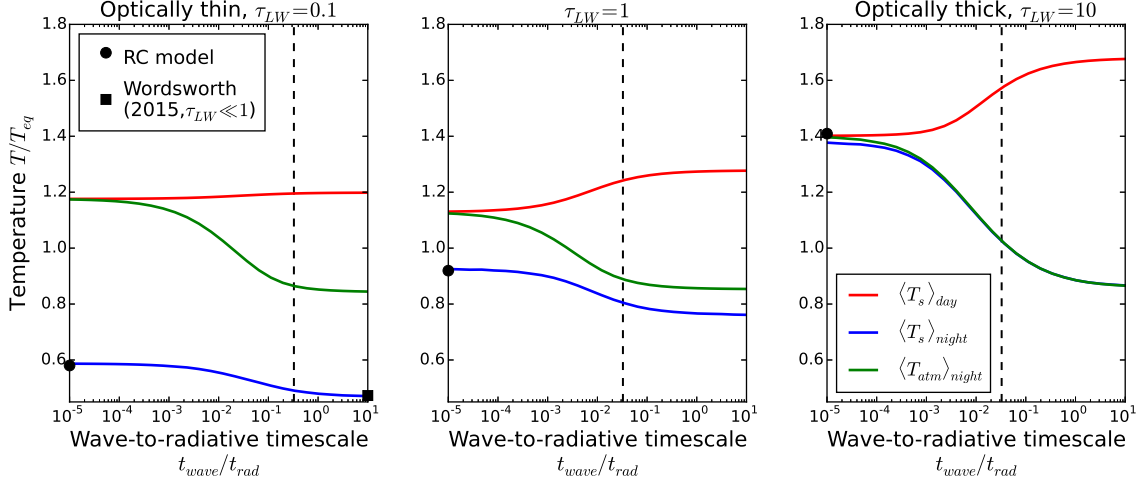


Figure 10. Day-night temperature gradients are large once the wave-to-radiative timescale ratio t_{wave}/t_{rad} exceeds the threshold from Equation 34 (vertical dashed lines). The panels show dayside surface temperature, $\langle T_s \rangle_{day}$, nightside surface temperature, $\langle T_s \rangle_{night}$, and the bottom-most atmospheric temperature on the nightside, $\langle T_{atm} \rangle_{night}$, from the radiative-convective-subsiding model (RCS, Section 5). In all cases, cool/thick atmospheres with $t_{wave}/t_{rad} \lesssim 10^{-4}$ have small temperature gradients between dayside surface and nightside atmosphere. Surface temperature gradients additionally depend on optical thickness, and even cool/thick atmospheres can have large day-night surface temperature gradients if $\tau_{LW} \ll 1$ (left panel). Black symbols show the nightside surface temperatures predicted by the radiative-convective model (RC), and the asymptotic scaling of Wordsworth (2015); the RCS model reduces to either in the limits $t_{wave}/t_{rad} \lesssim 10^{-4}$ and $t_{wave}/t_{rad} \gtrsim 1$.

where $\beta = R/(c_p n)$ sets the adiabatic lapse rate, $t_{sub} \equiv p_s/\bar{\omega}$ is a characteristic subsidence timescale for a parcel of air and $t_{rad} = p_s c_p / (g \sigma T_{eq}^3)$ is the radiative cooling timescale. Equation 27 is the three-dimensional equivalent of the WTG scaling developed by Perez-Becker & Showman (2013) using the shallow-water equations. The lapse rate parameter β is always of order unity whereas the subsidence timescale t_{sub} is an emergent timescale set by the large-scale dynamics. When $t_{sub}/t_{rad} \ll 1$ radiative cooling is inefficient compared with subsidence heating, the nightside atmosphere is close to an adiabat, and day-night temperature differences are small. When $t_{sub}/t_{rad} \gtrsim 1$ a parcel of air cools significantly as it descends, the nightside develops inversions, and day-night differences are large. Finally, for $t_{sub}/t_{rad} \gg 1$ the nightside is close to radiative equilibrium.

The transition to large day-night temperature gradients occurs at a wave-to-radiative timescale threshold of $t_{wave}/t_{rad} \sim 10^{-2}$. Figure 10 shows temperatures from the RCS model as a function of the timescale ratio t_{wave}/t_{rad} and optical thickness τ_{LW} . We assume a representative rocky planet scenario⁵, and plot the dayside surface temperature, $\langle T_s \rangle_{day}$, nightside surface temperature, $\langle T_s \rangle_{night}$, and the atmospheric temperature just above the nightside surface, $\langle T_{atm} \rangle_{night}$. Because the atmospheric temperature on the dayside is strongly coupled to the surface via convection, $\langle T_{atm} \rangle_{day} \approx \langle T_s \rangle_{day}$, the difference between $\langle T_s \rangle_{day}$ and $\langle T_{atm} \rangle_{night}$ also shows the day-night temperature gradient in the lowest part of the atmosphere. First, it is clear from Figure 10 that the atmospheric temperature gradient is small when $t_{wave}/t_{rad} \ll 10^{-2}$. The transition to large temperature gradients spans many orders of magnitude, but we take $t_{wave}/t_{rad} \sim 10^{-2}$ as a representative value that ensures temperature gradients are large for larger values of t_{wave}/t_{rad} . Second, once day-night atmospheric gradients are large their magnitude additionally depends on τ_{LW} , with optically thicker atmospheres having larger maximum temperature gradients (compare maximum difference between $\langle T_s \rangle_{day}$ and $\langle T_{atm} \rangle_{night}$). Third, because the nightside surface is in radiative equilibrium with the overlying atmosphere, the gradient in surface temperatures is at least as big as the gradient in atmospheric temperatures. However, it can be much larger in the optically thin limit because the nightside atmosphere becomes ineffective at radiatively heating the nightside surface. At low optical thickness the nightside surface is much colder than the overlying air (Fig. 10a), while at high optical thickness the nightside surface is closely tied to the overlying air temperature (Fig. 10c).

Next, we explain why atmospheres develop large temperature gradients at $t_{wave}/t_{rad} \sim 10^{-2}$. As we showed above, the nightside temperature structure is controlled by the ratio of subsidence to radiative timescales, t_{sub}/t_{rad} . Here we analyze the processes that control t_{sub} . Using the heat engine and the area ratio between upward and downward

⁵ We assume an Earth-sized planet, $a = a_{\oplus}$, with an N_2 -dominated atmosphere, $(R, c_p) = (R, c_p)_{N_2}$.

motions, we already found the pressure velocity on the nightside ω_{down} . Equation 26 allows us to write

$$t_{sub} = \frac{p_s}{\omega_{down}} = \frac{a}{\chi U_s}. \quad (28)$$

Next, we scale the surface wind speed U_s from the heat engine (Equation 12)

$$U_s = \left[(T_d/T_{eq} - 1) \times (1 - e^{-\tau_{LW}}) \left(\frac{c_p}{R} \right)^2 \frac{t_{drag}}{t_{rad}} \right]^{1/3} \times c_{wave},$$

$$U_s \approx \left(\frac{c_p}{R} \right)^{2/3} \left(\frac{t_{drag}}{t_{rad}} \right)^{1/3} \times c_{wave}, \quad (29)$$

where in the second step we assumed an optically thick atmosphere, $\tau_{LW} \geq 1$, so that all incoming stellar flux goes towards driving atmospheric motion, $1 - e^{-\tau_{LW}} \approx 1$. We also drop the dependence on the dayside temperature from $T_d/T_{eq} - 1$. We do so because in the optically thick limit T_d is approximately given by Equation 1, so $(T_d/T_{eq} - 1)^{1/3} \approx (\tau_{LW}^\beta \Gamma[1 + 4\beta]^{-1/4} - 1)^{1/3}$ which is always of order unity⁶. We combine Equations 28 and 29 and find

$$t_{sub} = \frac{1}{\chi} \left(\frac{R}{c_p} \right)^{2/3} \left(\frac{t_{rad}}{t_{drag}} \right)^{1/3} t_{wave} \quad (30)$$

Equation 30 gives us the subsidence time on the nightside. Day-night temperature gradients will be small if a parcel of air cools slower than it sinks, $t_{rad} > t_{sub}$. Conversely, day-night temperature gradients will be large if a parcel cools faster than it sinks, $t_{rad} < t_{sub}$. The threshold between these two regimes is

$$t_{rad} \sim t_{sub}$$

$$t_{rad} \sim \frac{1}{\chi} \left(\frac{R}{c_p} \right)^{2/3} \left(\frac{t_{rad}}{t_{drag}} \right)^{1/3} t_{wave}$$

$$t_{rad}^{2/3} \sim \frac{1}{\chi} \left(\frac{R}{c_p} \right)^{2/3} \left(\frac{1}{t_{drag}} \right)^{1/3} t_{wave}$$

$$t_{rad} \sim \left(\frac{1}{\chi} \right)^{3/2} \left(\frac{R}{c_p} \right) \left(\frac{t_{wave}}{t_{drag}} \right)^{1/2} t_{wave} \quad (\text{for } \tau_{LW} \geq 1). \quad (31)$$

We can find a similar threshold for optically thin atmospheres ($\tau_{LW} < 1$). We note that the standard radiative timescale $t_{rad} = c_p p_s / (g \sigma T_{eq}^3)$ is the cooling timescale of an *optically thick* column of air. In contrast, an optically thin column of air only emits a radiative flux $\sim \tau_{LW} \times \sigma T_{eq}^4$ so its radiative cooling timescale is

$$t_{rad,thin} = \frac{t_{rad}}{\tau_{LW}}. \quad (32)$$

WTG balance (Equation 27) in the optically thin regime is still governed by the ratio of subsidence to radiative timescales, but now t_{rad} has to be replaced by $t_{rad,thin}$.

To find the subsidence timescale t_{sub} in the optically thin limit, we note that optically thin atmospheres are also less efficient heat engines. The lower efficiency arises because, for $\tau_{LW} \ll 1$, the surface re-emits most of the incoming stellar flux directly back to space and only a fraction $1 - e^{-\tau_{LW}} = 1 - (1 - \tau_{LW} + \dots) \approx \tau_{LW}$ of the stellar flux is available to drive atmospheric motions. The dayside temperature T_d is approximately constant in the optically thin case (Fig. 3), so t_{sub} is

$$t_{sub} = \frac{1}{\chi} \left(\frac{R}{c_p} \right)^{2/3} \left(\frac{t_{rad,thin}}{t_{drag}} \right)^{1/3} t_{wave}. \quad (33)$$

Equation 33 only differs from Equation 30 through the use of $t_{rad,thin}$ instead of t_{rad} . Our result for large temperature gradients therefore also holds for optically thin atmospheres, once we replace t_{rad} with $t_{rad,thin}$.

To compare our result with the result for hot Jupiters, we express the criterion for an atmosphere to develop large temperature gradients in terms of the wave-to-radiative timescale ratio t_{wave}/t_{rad} . Day-night atmospheric temperature

⁶ For example, assuming $\tau_{LW} = 2$ and a diatomic gas without pressure broadening ($\beta = 2/7$), $(T_d/T_{eq} - 1)^{1/3} \approx 0.6$. The gamma function $\Gamma[1 + 4\beta]^{-1/4}$ does not vary significantly over the plausible range of atmospheric gases. Similarly, the dependency on $\tau_{LW}^{\beta/3}$ is negligible because the exponent $\beta/3$ is always small.

gradients are large once

$$\frac{t_{wave}}{t_{rad}} \gtrsim \begin{cases} \chi^{3/2} \times \frac{c_p}{R} \left(\frac{t_{drag}}{t_{wave}} \right)^{1/2} & \text{if } \tau_{LW} \geq 1, \\ \frac{\chi^{3/2}}{\tau_{LW}} \times \frac{c_p}{R} \left(\frac{t_{drag}}{t_{wave}} \right)^{1/2} & \text{if } \tau_{LW} < 1. \end{cases} \quad (34)$$

We emphasize that Equation 34 only ensures that atmospheric temperature gradients are large, but they remain significant until t_{wave}/t_{rad} becomes extremely small (Fig. 10).

We draw three important conclusions from Equation 34. First, in the optically thick case the right hand side is dominated by $\chi \approx 1/20$ (Section 5) while the other quantities do not vary much in most cases of interest. The small value of χ causes the threshold for large day-night temperature gradients to generally be much smaller than one. As a representative high mean-molecular-weight (MMW) scenario, we consider an N_2 atmosphere with $T_{eq} = 300$ K. In this case $c_p/R = 7/2$ and $t_{drag}/t_{wave} = 1.4$ (Appendix A), so temperature gradients are large when

$$\left(\frac{t_{wave}}{t_{rad}} \right)_{high\ MMW} \gtrsim 5 \times 10^{-2}. \quad (35)$$

Our result explains why rocky planets develop large atmospheric temperature gradients at a threshold almost two orders of magnitudes smaller than what one would expect based on the results for hot Jupiters, $t_{wave}/t_{rad} \gtrsim 1$.

Second, hot H_2 -dominated atmospheres are a notable exception to the first result and develop day-night temperature gradients at larger values of t_{wave}/t_{rad} . The larger threshold arises because H_2 -dominated atmospheres have larger scale heights than high-MMW atmospheres, which increases the drag time t_{drag} . For example, we consider a H_2 atmosphere with $T_{eq} = 600$ K. In this case $t_{drag}/t_{wave} = 40$ (Appendix A) so temperature gradients are large when

$$\left(\frac{t_{wave}}{t_{rad}} \right)_{H_2} \gtrsim 0.2. \quad (36)$$

The wave-to-radiative timescale threshold in this case is a factor of four larger than for high-MMW atmospheres, but it is still almost an order of magnitude smaller than the result for hot Jupiters, $t_{wave}/t_{rad} \gtrsim 1$.

Third, optically thin atmospheres are less prone to developing day-night temperature gradients than optically thick atmospheres because optically thin atmospheres cool less effectively. Although optically thin atmospheres are also less efficient heat engines, the radiative effect dominates because $t_{rad,thin} \propto 1/\tau_{LW}$ whereas $t_{sub} \propto t_{rad,thin}^{1/3} \propto 1/\tau_{LW}^{1/3}$. Weak-temperature-gradient (WTG) balance therefore holds even better in optically thin atmospheres than in optically thick ones. It also explains why the stratospheres of our simulations, where the atmosphere becomes optically thin (Robinson & Catling 2012), are much more horizontally homogeneous than the lower atmosphere (Fig. 1).

We can now relate the RCS model to the results in Section 3. First, when $t_{sub}/t_{rad} \ll 1$ radiative cooling is inefficient compared to subsidence heating. In this limit sinking parcels of air on the nightside remain close to an adiabat and the RCS model reduces to the RC model⁷. Figure 10 shows nightside surface temperatures in both models and demonstrates that the RCS model reduces to the RC model at a representative value of $t_{wave}/t_{rad} \lesssim 10^{-4}$ (compare blue lines to black dots). Second, when $t_{sub}/t_{rad} \gg 1$ radiative cooling is much stronger than subsidence heating. In this limit WTG balance (Eqn. 27) becomes $dF/d\tau \approx 0$, so the nightside is in purely radiative equilibrium and F is vertically constant. To still satisfy the nightside surface budget (Equation 21c), F has to be zero. The Schwarzschild equation (Eqn. 19b) shows that in this case $d(\sigma T^4)/d\tau \approx 0$ which means the nightside becomes vertically isothermal with a temperature that is set by the overlying tropopause temperature $T_{strat}(\tau_0)$. A lower bound for T_{strat} (see Eqn. 20) is given by the skin temperature $T_{skin} \equiv 2^{-1/4} T_{eq}$ (Pierrehumbert 2011b). In the optically thin limit the nightside surface energy budget is then equal to $\sigma T_n^4 = \tau_{LW} \times \sigma T_{skin}^4 = \tau_{LW} \times \sigma T_{eq}^4/2$, and we recover Wordsworth (2015)'s result $T_n = T_{eq}(\tau_{LW}/2)^{1/4}$. Figure 10 shows that the nightside temperature in the RCS model reduces to this limit at a representative value of $t_{wave}/t_{rad} \gtrsim 1$ (compare black square and blue line in left panel).

Up to now we have focused on slowly rotating planets $a^2/L_{Ro}^2 < 1$. Next, we consider the effects of rapid rotation, and how they interact with the threshold for large day-night temperature gradients.

⁷ Because the RCS model additionally includes a stratosphere, it predicts slightly colder nightsides in the limit $t_{wave}/t_{rad} < 10^{-4}$ than the RC model but the effect is small (the black dot is slightly above the blue line in Figure 10, right panel).

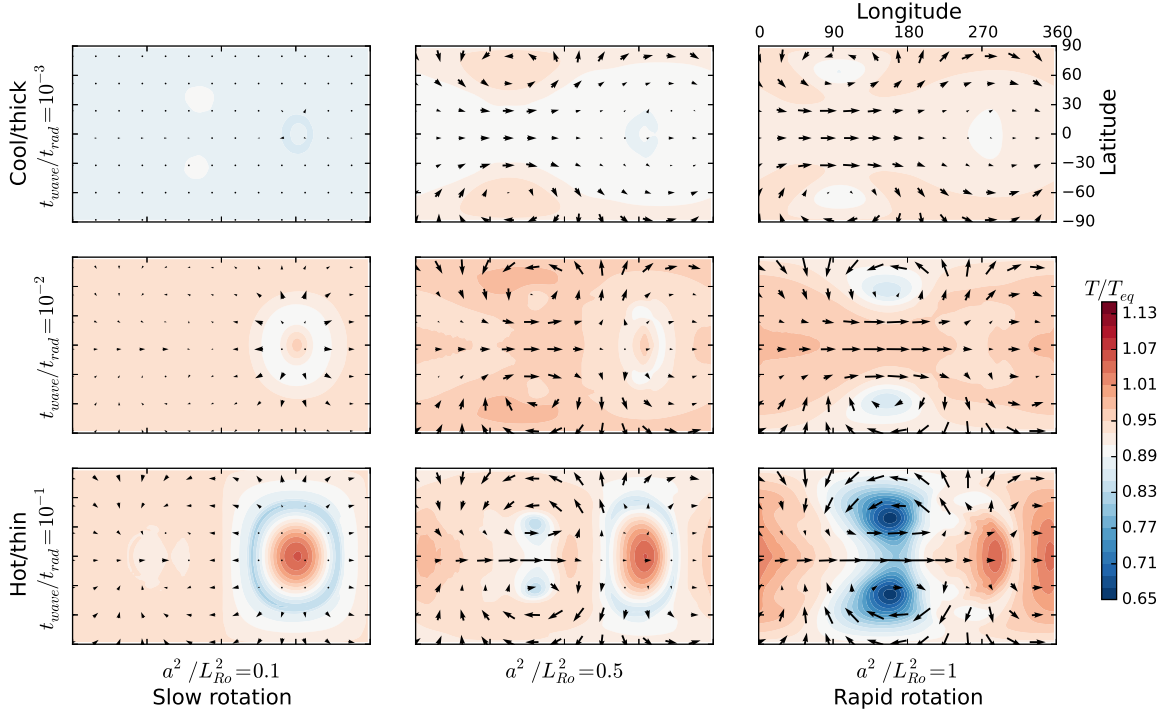


Figure 11. Rapid rotation ($a^2/L_{Ro}^2 \gtrsim 1$) does not have a strong effect on temperature structure unless the atmosphere is also hot or thin ($t_{wave}/t_{rad} > 10^{-2}$). Shown are 2D temperature and wind fields, averaged over the upper troposphere ($0.3 \leq p/p_s \leq 0.4$). Rotation increases from left to right, the wave-to-radiative timescale ratio increases from top to bottom. Increased rotation changes the circulation drastically, from a day-night flow at slow rotation (left) to an equatorially superrotating jet and cold nightside vortices at rapid rotation (right). However, at low t_{wave}/t_{rad} temperature gradients are small, even if rotation is rapid (top right). Large temperature gradients, eastward hot spot offsets, and cold nightside vortices only emerge once an atmosphere is both hot/thin and rotates rapidly (bottom right). The substellar point is located at 270° longitude.

7. EFFECTS OF RAPID ROTATION ON TEMPERATURE STRUCTURE

In this section we use GCM simulations to address how rapid rotation affects the circulation and temperature structure. [Leconte et al. \(2013\)](#) showed that tidally locked planets develop drastically different circulations when $a^2/L_{Ro}^2 \gtrsim 1$ because equatorial waves are not able to freely propagate into high latitudes once the planetary radius, a , is larger than the equatorial Rossby radius, L_{Ro} . Rapidly rotating planets then develop standing Rossby and Kelvin wave patterns. The standing wave patterns lead to strong equatorial superrotation, an eastward offset of the equatorial hot spot, and off-equatorial cold vortices on the nightside ([Matsuno 1966](#); [Showman & Polvani 2011](#)). Here we also find that the circulation regime changes at $a^2/L_{Ro}^2 \sim 1$. However, while rapid rotation drastically alters the flow field the effect on temperature structure is small unless the atmosphere is also prone to developing strong temperature gradients, $t_{wave}/t_{rad} \gtrsim \mathcal{O}(10^{-2})$.

We perform a set of GCM simulations in which we vary a^2/L_{Ro}^2 and t_{wave}/t_{rad} while keeping all other parameters fixed. We vary a^2/L_{Ro}^2 by changing the rotation rate Ω , and t_{wave}/t_{rad} by changing the surface pressure p_s . All other parameters are fixed to the same values as the reference simulation in Figure 1, that is, $a = a_\oplus$, $T_{eq} = 283\text{K}$, $(R, c_p) = (R, c_p)_{N_2}$, and $\tau_{LW} = 1$. We explore $a^2/L_{Ro}^2 = (0.1, 0.5, 1)$ and $t_{wave}/t_{rad} = (10^{-3}, 10^{-2}, 10^{-1})$, which correspond to $2\pi/60 \text{ days} \leq \Omega \leq 2\pi/6 \text{ days}$ and $5 \text{ bar} \leq p_s \leq 0.05 \text{ bar}$.

We find that rapid rotation has a large effect on the circulation, but its effect on the temperature structure is small unless t_{wave}/t_{rad} also exceeds the threshold $t_{wave}/t_{rad} \gtrsim 5 \times 10^{-2}$ from the previous section. Figure 11 shows 2D maps of the circulation and temperatures in the upper atmosphere. The wind and temperatures are mass-weighted averages taken over $0.3 \leq p/p_s \leq 0.4$, and the substellar point is located at longitude $\lambda = 270^\circ$. Slowly rotating simulations are shown in the left column of Figure 11. As expected, the circulation consists of a substellar-to-antistellar flow. At small values of t_{wave}/t_{rad} the day-night temperature differences are small, but the atmosphere develops large day-night temperature gradients at $t_{wave}/t_{rad} = 10^{-1}$, consistent with our results in Section 6. The top row of Figure 11 shows simulations with small t_{wave}/t_{rad} . As rotation rate increases, the atmospheric circulation changes drastically. A strong equatorial jet develops and the nightside atmosphere additionally develops standing Rossby waves in the

form of off-equatorial vortices (Showman & Polvani 2011). Nevertheless, as long as $t_{\text{wave}}/t_{\text{rad}} = 10^{-3}$, the maximum horizontal temperature difference at $a^2/L_{\text{Ro}}^2 = 1$ only reaches $0.05T_{\text{eq}}$, or ~ 15 K.

Figure 11 underlines that day-night atmospheric temperature gradients are primarily controlled by $t_{\text{wave}}/t_{\text{rad}}$. However, the effect of rapid rotation can strongly enhance temperature gradients in the form of eastward hot spot offsets and cold nightside vortices. The slowly rotating simulation with a thin atmosphere ($a^2/L_{\text{Ro}}^2 = 0.1$, $t_{\text{wave}}/t_{\text{rad}} = 10^{-1}$; bottom left) has its hottest point located at the substellar point and a maximum horizontal temperature difference of $0.2T_{\text{eq}}$, or ~ 65 K. In contrast, the simulation with the same value of $t_{\text{wave}}/t_{\text{rad}}$ but at rapid rotation shows an eastward hot spot offset and a significantly larger maximal horizontal temperature difference of $0.4T_{\text{eq}}$, or ~ 110 K (bottom right). In the following section we consider what our results imply for future observations.

8. IMPLICATIONS FOR OBSERVATIONS

Figure 12 summarizes some implications of our results for observations of rocky exoplanets. We showed that atmospheric day-night temperature contrasts strongly depend on the parameter $t_{\text{wave}}/t_{\text{rad}} = a/(\sqrt{R/c_p} \times \sqrt{RT_{\text{eq}}}) \times g\sigma T_{\text{eq}}^3/(c_p p_s) \propto T_{\text{eq}}^{5/2}/p_s$. The planetary radius a and surface gravity g vary relatively little for plausible rocky planets, which means day-night temperature differences are to first order controlled by the equilibrium temperature T_{eq} , the surface pressure p_s , and whether or not the atmosphere is made of H_2 (via R and c_p). In Figure 12 we consider these parameters for a GJ 1132b-sized planet⁸ with hypothetical CO_2 and H_2 atmospheres. The red region indicates when the atmosphere is hot/thin and develops large day-night atmospheric temperature gradients (Equation 34 for $\tau_{\text{LW}} \geq 1$). The blue region indicates when the atmosphere is cool/thick and day-night atmospheric temperature gradients become negligible ($t_{\text{wave}}/t_{\text{rad}} \leq 10^{-4}$ from Section 6). Part of the CO_2 phase space is unstable to atmospheric collapse, which occurs when the nightside surface is cold enough for CO_2 to condense. We delineate atmospheric collapse using two approaches. First, the solid black line shows the empirical fit from Wordsworth (2015), who used a GCM with full radiative transfer to compute collapse thresholds up to $T_{\text{eq}} = 367$ K. Second, we use the RCS model to compute when nightside surface temperatures fall below the condensation temperature of CO_2 . To specify the optical thickness we use Equation 6 and assume $\tau(1 \text{ bar}) = 1$ and $n = 1$. Although we do not include non-grey effects, the RCS model (dashed black line) closely fits the GCM results (solid black line) over the range of parameters explored by Wordsworth (2015). As such, we consider the RCS model appropriate for predicting atmospheric collapse (also see Section 9). We repeat a similar computation for H_2 atmospheres, and find that the entire phase space in Figure 12b is stable against

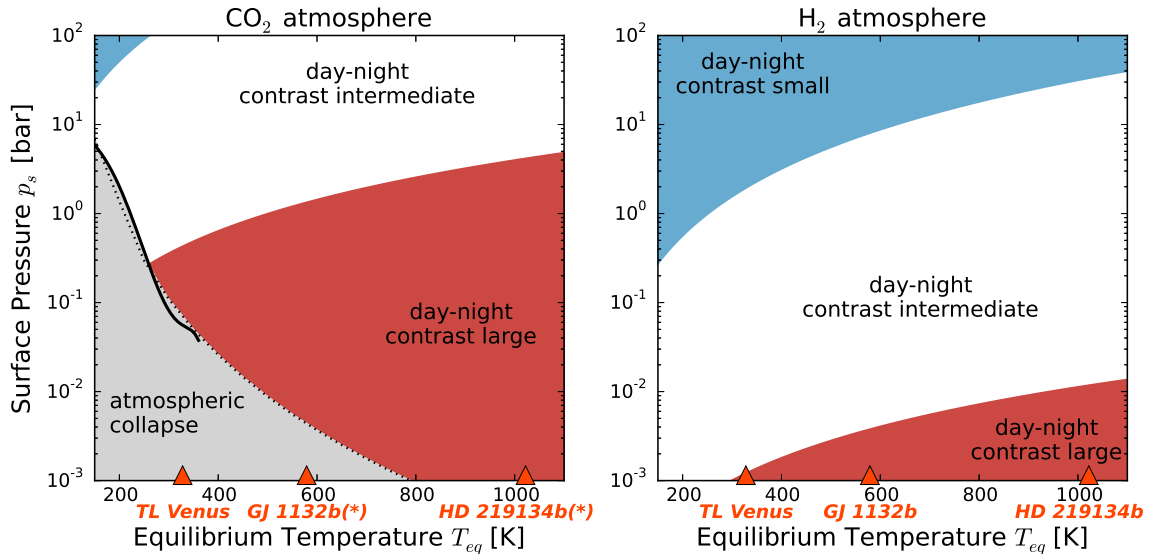


Figure 12. CO_2 atmospheres are more likely to develop large temperature gradients than H_2 atmospheres. Atmospheric day-night temperature gradients are negligible inside the blue region ($t_{\text{wave}}/t_{\text{rad}} \leq 10^{-4}$) and are large inside the red region (Eqn. 34 for $\tau_{\text{LW}} \geq 1$). CO_2 atmospheres collapse inside the grey region [solid line: empirical fit to GCM results from Wordsworth (2015); dotted line: calculated using our RCS model]. Bottom symbols show equilibrium temperatures of two nearby rocky planets and of a hypothetical tidally locked Venus; (*) marks scenarios for which rotational effects would additionally be important ($a^2/L_{\text{Ro}}^2 \geq 1$). The shown thresholds assume a GJ1132b-sized planet ($a, g = 1.16a_{\oplus}, 11.7 \text{ m s}^{-2}$).

⁸ We assume $a, g = 1.16a_{\oplus}, 11.7 \text{ m s}^{-2}$ (Berta-Thompson et al. 2015).

collapse⁹. The symbols at the bottom of Figure 12 show equilibrium temperatures¹⁰ of two recently-discovered rocky planets and of a hypothetical tidally locked planet at Venus’ present-day orbit (Berta-Thompson et al. 2015; Motalebi et al. 2015). Finally, we found that temperature structure can be affected by rapid rotation. We mark all rapidly rotating planet scenarios with $a^2/L_{Ro} \geq 1$ using star symbols (*). For these cases we expect that strong rotational effects, such as large eastward hot spot offsets or cold nightside vortices, occur inside the red region (see Section 7).

Figure 12 allows us to make some tentative predictions. First, with a high MMW atmosphere like CO₂, GJ 1132b and HD 219134b would have non-negligible day-night temperature gradients. This conclusion holds even for surface pressures as high as that of Venus ($p_s = 92$ bar). Second, GJ 1132b and HD 219134b with CO₂ atmospheres both satisfy the criterion for rapid rotation ($a^2/L_{Ro}^2 \geq 1$). Should observations detect a large eastward hot spot offset, it would favor surface pressures less than $\mathcal{O}(1)$ bar (inside the red region). Third, Figure 12a shows that a CO₂ atmosphere with surface pressure comparable to that of Mars ($p_s = 6 \times 10^{-3}$ bar) would be close to collapse on GJ 1132b. We note that our collapse calculation does not account for rotational effects, and cold nightside vortices (Fig. 11) would allow the atmosphere to collapse at even higher pressures. Fourth, if these planets managed to retain H₂-dominated atmospheres against atmospheric escape, they would be stable against collapse and exhibit much smaller day-night temperature differences than similar CO₂ atmospheres. The increased stability and smaller temperature gradient is due to a combination of H₂’s large heat capacity c_p , which increases the radiative timescale t_{rad} (Menou 2012a), its large gas constant R , which increases the speed of atmospheric waves c_{wave} and thus decreases the wave timescale t_{wave} (Heng & Kopparla 2012), and its increased scale height, which decreases the effect of friction (Appendix A). Fifth, H₂-dominated atmospheres would be significantly less affected by rotation than CO₂ atmospheres. The smaller effect of rotation is also due to the reduced wave timescale t_{wave} in H₂ atmospheres. For example, assuming GJ 1132b’s equilibrium temperature $T_{eq} = 579$ K, the characteristic speed of gravity waves in a CO₂ atmosphere is $c_{wave} = \sqrt{R/c_p} \times \sqrt{RT_{eq}} = 158$ m s⁻¹, whereas in a H₂ atmosphere $c_{wave} = 838$ m s⁻¹. It follows that the nondimensional Rossby radius, $a^2/L_{Ro}^2 = 2\Omega a/c_{wave}$, is about five times smaller in a H₂ atmosphere. Our results also imply that rocky planets with H₂-dominated atmospheres are less likely to exhibit eastward hot spot offsets and cold nightside vortices. These predictions are qualitative because they do not consider the optical thickness τ_{LW} , which helps set the magnitude of the day-night temperature gradient (Fig. 10). Quantitatively interpreting an observed day-night temperature gradient also requires constraining τ_{LW} , for example via transit spectroscopy (see Koll & Abbot 2015).

One way of distinguishing the scenarios in Figure 12 would thus be through combined transit spectroscopy and thermal phase curve observations with *JWST*. Previous feasibility studies have tended to emphasize the transit technique (e.g., Beichman et al. 2014; Batalha et al. 2015), here we compare the signal-to-noise ratio (SNR) that can be achieved by spending the same amount of *JWST* time on low spectral-resolution transit and broadband phase curve observations. We find that it would take about as much time to measure the broadband mid-IR phase curve of a short-period rocky exoplanet as it would to detect molecular signatures in its atmospheres through near-IR transit spectroscopy. The basic science goal for transit observations would be to detect a molecular species from its spectral imprint; a flat spectrum could alternately be a cloudy atmosphere or no atmosphere. The basic science goal for phase curve observations would be to detect the day-night flux difference of a bare rock. An observed flux difference lower than that of a bare rock would imply the presence of an atmosphere thick enough to modify the day-night temperature contrast (outside the red region in Fig. 12). Similarly, hot/cold spot offsets would imply the presence of an atmosphere that is hot or thin enough that its thermal structure is significantly affected by rotation (see above). We consider GJ 1132b with a CO₂-dominated atmosphere as a representative target. We assume GJ 1132b is tidally locked, which could be verified using optical phase curves with *TESS* (cf. Fujii et al. 2014). We compute transit signals following Cowan et al. (2015), but assume that spectral features in the near-IR cause an absorption difference of three scale heights and have a typical width of $0.1\mu\text{m}$ (see Table 2, Kaltenecker & Traub 2009). We compute the phase curve signal of a bare rock following Koll & Abbot (2015). We estimate *JWST*’s precision in the near-IR ($1 - 4\mu\text{m}$ in $0.1\mu\text{m}$ bins, $R \sim 25$ on NIRSpec) using the photon noise limit (see Koll & Abbot 2015). We similarly estimate the precision in the mid-IR ($16.5 - 19.5\mu\text{m}$ broadband, F1800W on MIRI) assuming photon noise, but account for the imperfect instrument throughput of $1/3$ (Glasse et al. 2010). We assume that both techniques bin photons over the length of one transit (45 minutes) and we multiply the noise by $\sqrt{2}$ to account for the fact that both techniques compare two snapshots in time. We assume that a single transit measurement consists of observing the primary eclipse and an

⁹ We use the Solar opacity value in Menou (2012a) and $n = 1$, and compute nightside surface temperatures with the RCS model. We find that nightside temperatures always exceed the critical point of H₂, 33.2 K.

¹⁰ We assume a planetary albedo of zero.

Transit vs. phase curve observations of GJ 1132b with *JWST*

Method	Observation Time	Signal (ppm)	Noise (ppm)	SNR
Single transit ^a	one transit ^b = 90 min	19.9	19.7	1
Stacked transits ^a	13 transits = 19.5 hours	19.9	5.5	4
Thermal phase curve ^c	one half-orbit = 19.5 hours	373	84	4

^a 1 – 4 μm , NIRSpec, $R \sim 25$, CO₂-dominated atmosphere.

^b We assume a measurement lasts 45 min in-transit, plus 45 min out-of-transit baseline.

^c 16.5 – 19.5 μm , MIRI, broadband.

Table 2. Transit spectroscopy and thermal phase curve measurements of a planet like GJ 1132b will require similar amounts of *JWST* observation time. The shown signal-to-noise (SNR) ratios are estimates for the most basic observational goals: detecting molecular features in low-resolution near-IR transit spectra, and detecting the day-night thermal emission contrast of a bare rock in the mid-IR. We compute signals following Cowan et al. (2015) and Koll & Abbot (2015). We estimate noise assuming photon-limited precision, but include imperfect instrument throughput for MIRI (see Section 8).

equal out-of-transit baseline (cf. Kreidberg et al. 2014). We check our transit estimate by comparing our SNR with the detailed calculations in Batalha et al. (2015), and find that we can reproduce their results up to a factor of two (not shown). We also note that our estimate of GJ 1132b’s thermal emission is slightly higher than the signal in Berta-Thompson et al. (2015), because the observer-projected dayside temperature of a bare rock is higher than its equilibrium temperature by $(8/3)^{1/4} \approx 1.28$ (Koll & Abbot 2015).

Table 2 shows our results. Similar to previous estimates (e.g., Batalha et al. 2015; Cowan et al. 2015), we find that a single transit would not be sufficient to conclusively identify molecular absorption features (SNR ~ 1). The low SNR arises largely because of the high MMW atmosphere; for comparison, a H₂ atmosphere on GJ 1132b should be detectable in a single transit with SNR ~ 22 . For a CO₂ atmosphere, 13 repeated transit observations would reduce the noise sufficiently to allow spectral features to be discerned with SNR ~ 4 . The time it takes to measure 13 repeated transits of GJ 1132b is also equal to the time it takes to measure one half-orbit phase curve (from transit to secondary eclipse). We find that the thermal emission of a bare rock would be detectable with a comparable SNR ~ 4 . We conclude that characterizing high MMW atmospheres of rocky exoplanets will require relatively large investments of *JWST* time. If such observations are pursued, however, then thermal phase curves are a feasible technique that would yield important complementary information about these planets (Koll & Abbot 2015).

9. DISCUSSION

The heat engine framework is well-established for Earth’s atmosphere (e.g., Peixoto & Oort 1984). Similarly Goodman (2009) pointed out that hot Jupiters can be viewed as heat engines, but did not develop his insight more quantitatively. Here we have demonstrated that the atmospheres of rocky exoplanets act as heat engines, which allowed us to develop a new constraint on their day-night circulations. We also found that surface wind speeds in most of our GCM simulations are about a factor of two smaller than the value predicted by the heat engine (Fig. 6). Because work scales with the cube of the surface wind speed, our simulations produce $\sim (1/2)^3 = 1/8$ as much work as an ideal heat engine. Interestingly, Earth’s atmospheric heat engine also produces about an order of magnitude less work than its ideal limit and therefore has a similar inefficiency as our dry and tidally locked simulations (Peixoto & Oort 1984). Our result seems to be at odds with the usual understanding that the inefficiency of Earth’s atmospheric heat engine is caused by its hydrological cycle (Pauluis et al. 2000; Pauluis 2010), and also raises the question whether our scaling can be generalized to planets that are not tidally locked. We hope to address these issues in future work. Our results also strongly suggest that hot Jupiters should obey similar constraints as rocky planets. For example, using the heat engine framework it might be possible to constrain the day-night overturning circulation, which controls the vertical mixing and chemical equilibrium of hot Jupiter atmospheres. However, modeling these atmospheres as heat engines will require a better understanding of the mechanisms through which they dissipate kinetic energy, which could include magneto-hydrodynamic drag, shocks, or shear instabilities (Li & Goodman 2010; Menou 2012b; Fromang et al. 2016).

Our results allow us to interpret previous GCM results that have not been fully explained yet. First, Merlis & Schneider (2010) explored Earth-like atmospheres at different rotation rates. They found that although the strength of superrotation is strongly dependent on rotation rate, day-night surface temperature gradients are mostly insensitive to rotation rate (their Fig. 15). Our results explain why: Merlis & Schneider varied rotation rates while keeping the stellar flux fixed at Earth’s value. Their simulations were therefore in the rapidly rotating ($a^2/L_{Ro}^2 > 1$) but relatively cool/thick regime ($t_{wave}/t_{rad} < 10^{-2}$) in which temperature structure is not strongly sensitive to rotation (Fig. 11).

Second, in [Koll & Abbot \(2015\)](#) we found that thermal phase curves are mainly sensitive to the nondimensional parameters $t_{\text{wave}}/t_{\text{rad}}$ and τ_{LW} . Our result only broke down for hot/thin and rapidly rotating atmospheres, $t_{\text{wave}}/t_{\text{rad}} \gtrsim 10^{-2}$ and $a^2/L_{\text{Ro}}^2 \gtrsim 1$. Our results here explain both the wave-to-radiative timescale threshold of $t_{\text{wave}}/t_{\text{rad}} \sim 10^{-2}$ and why rotation is relatively unimportant (Figs. 10 and 11).

There are additional physical effects that might affect our conclusions. We assume broadband grey radiative transfer, but a wide range of plausible atmospheric compositions feature significant spectral window regions. As already noted by [Leconte et al. \(2013\)](#) and [Wordsworth \(2015\)](#), window regions allow the nightside surface to cool even more effectively, which would increase day-night surface temperature gradients compared to that predicted by our grey models. At the same time, large spectral window regions would increase the atmosphere’s radiative cooling timescale and thus reduce atmospheric temperature gradients, similar to the optically thin cases we discussed in Section 6. We also did not consider shortwave absorption. Shortwave absorption will shift heating to lower pressures, which would decrease the heat intake temperature of the atmospheric heat engine and reduce the atmospheric circulation strength. We therefore expect our heat engine theory to be an upper bound on wind speeds.

Many planets might be able to retain a hydrologic cycle (e.g., H_2O inside the habitable zone, or CH_4 on Titan-like planets) against atmospheric escape and nightside collapse. Besides changing the atmosphere’s radiative properties (e.g., H_2O effectively absorbs both in the shortwave and longwave), condensation would also modify the atmospheric dynamics. Moist GCM simulations indicate that the temperature and circulation structure sketched out in Figure 8 could still apply qualitatively ([Merlis & Schneider 2010](#); [Yang et al. 2013](#)), but with several modifications. First, latent heat transport would reduce the day-night temperature gradient compared to dry atmospheres ([Leconte et al. 2013](#)). Second, moist convection would lead to thick cloud cover on the dayside and could drastically change a planet’s appearance to remote observers ([Fortney 2005](#); [Yang et al. 2013](#)). Third, dry atmospheres develop strongly turbulent daysides. The friction associated with this dry convection allows the nightside temperature structure to decouple from regions of convection (Fig. 1, [Voigt et al. 2012](#)). In contrast, moist atmospheres such as Earth’s tropics maintain an adiabatic temperature profile through deep moist convection, while the dry turbulent boundary layer is relatively shallow. We therefore expect that moist atmospheres would be less dominated by friction, and would be even better captured by WTG models similar to our radiative-convective model (Section 3).

It is an open question how many rocky planets around M-stars will actually be tidally locked. [Leconte et al. \(2015\)](#) found that thermal tides in relatively thick atmospheres ($p_s \gtrsim 1$ bar) can prevent habitable-zone planets around early M-dwarfs from reaching a tidally locked state. Although thermal tides could limit the application of our results to planets on longer-period orbits, they are less likely to apply to planets around late M-dwarfs or hot exoplanets like GJ 1132b. Moreover, given that rocky exoplanets are extremely common, we also expect that future discoveries will find rocky exoplanets in a wide range of rotational states. Optical phase curves could constrain the rotation rates of these planets without relying on models ([Fujii et al. 2014](#)), while future theoretical work should consider the connection between the tidally locked limit we considered here and planets in higher-order spin-orbit resonances.

10. CONCLUSIONS

We have developed a series of theoretical models to understand the basic temperature structure and large-scale circulations of tidally locked planets with dry atmospheres. These models are able to capture and predict many fundamental aspects of much more complex GCM simulations, including the atmospheric temperature structure, dayside and nightside surface temperatures, as well as large-scale wind speeds. We draw the following conclusions from our work:

1. Our radiative-convective model describes tidally locked atmospheres with efficient day-night heat transport and applies in the limit of cool and thick atmospheres ($t_{\text{wave}}/t_{\text{rad}} \lesssim 10^{-4}$). It captures the basic temperature structure of tidally locked planets and extends the asymptotic theory for optically thick atmospheres ($\tau_{\text{LW}} \gg 1$, [Pierrehumbert 2011b](#)) to arbitrary optical thickness.
2. Atmospheres of dry, tidally locked exoplanets act as global heat engines. Our heat engine scaling places strong constraints on the day-night circulation strength of tidally locked atmospheres.
3. Our radiative-convective-subsiding model describes tidally locked atmospheres with limited day-night heat transport. It extends both our radiative-convective model and the asymptotic theory for optically thin atmospheres ($\tau_{\text{LW}} \ll 1$, [Wordsworth 2015](#)), and captures the dynamics of a wide range of complex GCM simulations. It breaks down in the limit of atmospheres that are both rapidly rotating ($a^2/L_{\text{Ro}}^2 \gtrsim 1$) and hot/thin ($t_{\text{wave}}/t_{\text{rad}} > \mathcal{O}(10^{-2})$).

4. Like hot Jupiters, day-night atmospheric temperature gradients of rocky exoplanets become large once parcels of air take longer to subside than to cool radiatively. Unlike hot Jupiters, the timescale for subsidence on rocky planets is severely increased by the limited heat engine efficiency and the areal asymmetry between convection and subsidence. Rocky planets develop large day-night atmospheric temperature gradients when

$$\frac{t_{wave}}{t_{rad}} \gtrsim \begin{cases} \chi^{3/2} \times \frac{c_p}{R} \left(\frac{t_{drag}}{t_{wave}} \right)^{1/2} & \text{if } \tau_{LW} \geq 1, \\ \frac{\chi^{3/2}}{\tau_{LW}} \times \frac{c_p}{R} \left(\frac{t_{drag}}{t_{wave}} \right)^{1/2} & \text{if } \tau_{LW} < 1. \end{cases} \quad (37)$$

Optically thin atmospheres cool inefficiently, which makes them less likely to develop large temperature gradients than optically thick atmospheres.

5. Rapid rotation ($a^2/L_{Ro}^2 \gtrsim 1$) only has a strong influence on temperature structure if the wave-to-radiative timescale exceeds the above ratio, $t_{wave}/t_{rad} \gtrsim \mathcal{O}(10^{-2})$. Once rotation is important its effects cannot be ignored for a detailed understanding of a planet's atmosphere, including its thermal phase curve signature and the potential for atmospheric collapse.
6. Short-period rocky exoplanets with high MMW atmospheres and surface pressures of $\lesssim 1$ bar will likely exhibit significant day-night temperature gradients. Thermal phase curve observations of such planets will require similar amounts of *JWST* time as transit observations.

Our work was completed with resources provided by the University of Chicago Research Computing Center. We thank Malte Jansen and Feng Ding for insightful discussions, and an anonymous reviewer for their feedback. D.D.B. Koll was supported by a William Rainey Harper dissertation fellowship.

APPENDIX

A. APPENDIX: DRAG TIMESCALE

We start with the nondimensional parameters that we derived in [Koll & Abbot \(2015\)](#):

$$\left(\frac{R}{c_p}, \frac{a^2}{L_{Ro}^2}, \frac{t_{wave}}{t_{rad}}, \tau_{SW}, \tau_{LW}, \frac{C_D a}{H} \right). \quad (\text{A1})$$

Theoretical work on the atmospheric dynamics of hot Jupiters uses similar wave and radiative timescales (e.g., [Perez-Becker & Showman 2013](#)), but additionally introduces a drag timescale. This is because the drag mechanisms on hot Jupiters are still not well-constrained, and friction is often parametrized as Rayleigh friction with a unknown damping timescale. To facilitate comparison of our work with the hot Jupiter literature and to examine the importance of drag in the atmospheres of rocky planets, we rewrite the last of our six nondimensional parameters as a ratio of wave over drag timescales.

Models of terrestrial atmospheres (including FMS) often parametrize boundary layer friction as vertical momentum diffusion with a source term that is quadratic in wind speed. The horizontal momentum equation takes the form

$$\frac{D\mathbf{u}}{Dt} = \dots + g \frac{\partial \mathcal{D}_m}{\partial p}, \quad (\text{A2})$$

where \mathbf{u} is the horizontal wind speed, \mathcal{D}_m is the diffusive momentum flux due to surface drag, and the source term is $\mathcal{D}_m(p_s) = C_D \rho_s |\mathbf{u}_s| \mathbf{u}_s$. We take a vertical average across the boundary layer to find the average acceleration due to drag:

$$\begin{aligned} \frac{1}{p_s - p_{BL}} \int_{p_{BL}}^{p_s} \frac{D\mathbf{u}}{Dt} dp &= \dots + \frac{g}{p_s - p_{BL}} \int_{p_{BL}}^{p_s} \frac{\partial \mathcal{D}_m}{\partial p} dp \\ \overline{\frac{D\mathbf{u}}{Dt}} &= \dots + \frac{g}{p_s - p_{BL}} \times [\mathcal{D}_m(p_s) - \mathcal{D}_m(p_{BL})] \\ \overline{\frac{D\mathbf{u}}{Dt}} &= \dots + \frac{g \mathcal{D}_m(p_s)}{p_s - p_{BL}} \\ \overline{\frac{D\mathbf{u}}{Dt}} &= \dots + \frac{g C_D \rho_s |\mathbf{u}_s| \mathbf{u}_s}{p_s - p_{BL}} \end{aligned} \quad (\text{A3})$$

Here p_{BL} denotes the top pressure level of the boundary layer and we used the fact that drag has to disappear at the upper edge of the boundary layer, $\mathcal{D}_m(p_{BL}) = 0$. We then scale this equation for fast atmospheric motions $\mathbf{u} \sim c_{wave}$,

$$\begin{aligned} \frac{c_{wave}}{t_{drag}} &\sim \frac{g C_D \rho_s c_{wave}^2}{p_s} \\ \frac{c_{wave}}{t_{drag}} &\sim \frac{a C_D g}{R T_s} \frac{c_{wave}}{a} c_{wave} \\ \frac{c_{wave}}{t_{drag}} &\sim \frac{C_D a}{H} \frac{1}{t_{wave}} c_{wave}, \end{aligned} \quad (\text{A4})$$

where we have assumed that the boundary layer is thick, $p_{BL} \ll p_s$ (see Fig. 1), used the ideal gas law in the second step, $\rho_s = p_s R^{-1} T_s^{-1}$, and used the wave timescale $t_{wave} = a/c_{wave}$ in the last step. This lets us derive a drag timescale

$$t_{drag} \sim \frac{H}{C_D a} t_{wave}. \quad (\text{A5})$$

Note, in contrast to Rayleigh drag schemes where the drag timescale is independent of \mathbf{u} , here the drag timescale scales with \mathbf{u} and thus with the dynamical timescale t_{wave} . Using this drag timescale we can rewrite the last nondimensional parameter as $C_D a/H \sim t_{wave}/t_{drag}$ and find an alternative set of six governing parameters:

$$\left(\frac{R}{c_p}, \frac{a^2}{L_{Ro}^2}, \frac{t_{wave}}{t_{rad}}, \tau_{SW}, \tau_{LW}, \frac{t_{wave}}{t_{drag}} \right). \quad (\text{A6})$$

In most cases $C_D a/H$ is of order unity so the drag timescale is generally comparable to the dynamical timescale. For example, assuming a planet of Earth's size, $(a, g) = (a_\oplus, g_\oplus)$, a high MMW atmosphere, $R = R_{N_2}$, a relatively

cool temperature, $T_{eq} = 300K$, and a standard value for the drag coefficient, $C_D = 10^{-3}$, we find $t_{drag} = 1.4t_{wave}$. Variations in the planetary radius a or in the drag coefficient C_D do not affect this result much. For example, for a neutrally buoyant boundary layer $C_D = [k_{vk}/\log(z/z_0)]^2$, where k_{vk} is the von Karman constant, z is the height above the surface and z_0 is the surface roughness length. Because C_D only depends logarithmically on z_0 , the drag timescale is not very sensitive to the surface properties. This means we expect friction to generally be an important process inside the boundary layer of rocky planets.

The most important exception is a hot H_2 atmosphere, through its effect on the scale height H . For example, repeating the above calculation with a hot H_2 -dominated atmosphere, $R = R_{H_2}$ and $T_{eq} = 600$ K, we find $t_{drag} = 40t_{wave}$. This means surface friction is far less effective in H_2 atmospheres than in high MMW atmospheres.

B. APPENDIX: WIND SPEED SCALING FROM WORDSWORTH (2015)

To compare the results of [Wordsworth \(2015\)](#) with our GCM simulations we write [Wordsworth's](#) Equation 33 as

$$U_0 = 4\sigma T_{eq}^4 \frac{\tau_{LW}}{2\zeta p_s C_D c_p} \frac{R}{c_p}, \quad (B7)$$

where $\zeta \equiv 1/3$. The above equation reduces to [Wordsworth's](#) Equation 33 by plugging in his Equation 12, i.e., by assuming a specific form for τ . We leave the equation in this general form. We identify [Wordsworth's](#) absorbed stellar flux $(1-A)F$ as $4\sigma T_{eq}^4$.

The nondimensional equations in [Wordsworth \(2015\)](#) are not affected. To find the surface wind speed we solve his Equations 44 and 45 numerically to find \tilde{T} and \tilde{U} . We then convert the nondimensional \tilde{U} into a dimensional quantity using the above scale U_0 , i.e., $|\mathbf{u}| = U_0 \tilde{U}$.

C. APPENDIX: NUMERICAL SOLUTION FOR THE RCS MODEL

The boundary conditions of the radiative-convective-subsiding (RCS) model are specified at two different points, the tropopause and the surface. Instead of matching both boundaries simultaneously we first guess a value of the nightside OLR, $F(\tau_0)$. Given a value of $F(\tau_0)$, we can solve for all variables (T_d , τ_0 , $T(\tau)$, and $F(\tau)$). Our guess will in general not satisfy the nightside surface energy budget (Equation 21c), so we iterate until $F(\tau_{LW}) = 0$ is satisfied. To iterate we use a bisection method, where the nightside OLR is bounded by $0 \leq F(\tau_0) \leq \sigma T_{eq}^4$ (the limits correspond to a planet with zero and perfect day-night heat redistribution).

We proceed as follows. Given a value of $F(\tau_0)$, Equations 25 and 22 can be rewritten as an implicit equation for τ_0 ,

$$2 + \frac{\tau_0}{2} = \left(\frac{1 + \tau_0}{2}\right) \left(\frac{\tau_{LW}}{\tau_0}\right)^{4\beta} \left[e^{-(\tau_{LW} - \tau_0)} + \int_{\tau_0}^{\tau_{LW}} \left(\frac{\tau'}{\tau_{LW}}\right)^{4\beta} e^{-(\tau' - \tau_0)} d\tau' \right] + \frac{F(\tau_0)}{\sigma T_{eq}^4} \quad (C8)$$

We solve for τ_0 using, again, a bisection method, where we note that $0 < \tau_0 < \tau_{LW}$. We then use Equations 20 and 22 to find $T(\tau_0)$ and T_d :

$$T(\tau_0) = T_{eq} \left(\frac{1 + \tau_0}{2}\right)^{1/4} \quad (C9)$$

$$T_d = T_{eq} \left(\frac{1 + \tau_0}{2}\right)^{1/4} \left(\frac{\tau_{LW}}{\tau_0}\right)^\beta. \quad (C10)$$

Once we know T_d we can find $\bar{\omega}$ (Equations 12 and 26). We then have three boundary conditions that are specified at the upper boundary, the guessed $F(\tau_0)$, $dF(\tau_0)/d\tau = 0$, and $T(\tau_0)$. We use SciPy's VODE solver to integrate the WTG and Schwarzschild equations (Equations 19) down to the nightside surface, which gives us the net surface flux $F(\tau_{LW})$. We iterate until we satisfy the nightside surface budget, $F(\tau_{LW}) = 0$. After having solved for $T(\tau)$ we find the nightside surface temperature T_n using the nightside surface energy budget (cf. [Robinson & Catling 2012](#)),

$$\begin{aligned} \sigma T_n^4 &= F^-(\tau_{LW}) \\ &= \sigma T_{eq}^4 \frac{\tau_0}{2} e^{-(\tau_{LW} - \tau_0)} + \int_{\tau_0}^{\tau_{LW}} \sigma T(\tau')^4 e^{-(\tau' - \tau_0)} d\tau'. \end{aligned} \quad (C11)$$

D. APPENDIX: EQUATIONS OF MOTION

The FMS GCM integrates the primitive equations in pressure coordinates, which are

$$\frac{D\mathbf{u}}{Dt} = -f\mathbf{k} \times \mathbf{u} - \nabla\phi - g\frac{\partial\mathcal{D}_m}{\partial p}, \quad (\text{D12})$$

$$\frac{\partial\phi}{\partial p} = -\frac{RT}{p}, \quad (\text{D13})$$

$$\nabla \cdot \mathbf{u} + \frac{\partial\omega}{\partial p} = 0, \quad (\text{D14})$$

$$\frac{DT}{Dt} = \frac{RT\omega}{c_p p} + \frac{g}{c_p} \frac{\partial F}{\partial p} + \frac{g}{c_p} \frac{\partial\mathcal{D}}{\partial p}. \quad (\text{D15})$$

Here $\mathbf{u} = (u, v)$ is the horizontal wind velocity, $\frac{D}{Dt} = \frac{\partial}{\partial t} + \mathbf{u} \cdot \nabla + \omega \frac{\partial}{\partial p}$ is the material derivative, $f = 2\Omega \sin\theta$ is the Coriolis parameter, \mathbf{k} is local vertical unit vector, ϕ is the geopotential, T is temperature, $\omega \equiv Dp/Dt$ is the pressure velocity, \mathcal{D}_m and \mathcal{D} are the vertical diffusive fluxes of momentum and energy in the boundary layer, F is the net longwave flux, and an overview of the dimensional parameters can be found in Table 1. From the top, these equations express conservation of momentum, the hydrostatic approximation, conservation of mass, and conservation of energy. The net longwave flux F is governed by the two-stream Schwarzschild equations. For a grey gas these can be written in optical depth coordinates as

$$\frac{\partial^2 F}{\partial\tau^2} - F = -2\frac{\partial(\sigma T^4)}{\partial\tau}. \quad (\text{D16})$$

REFERENCES

- Abe, Y., Abe-Ouchi, A., Sleep, N. H., & Zahnle, K. J. 2011, *Astrobiology*, 11, 443
- Batalha, N., Kalirai, J., Lunine, J., Clampin, M., & Lindler, D. 2015, arXiv:1507.02655 [astro-ph], arXiv:1507.02655
- Beichman, C., Benneke, B., Knutson, H., et al. 2014, *Publications of the Astronomical Society of the Pacific*, 126, 1134
- Berta-Thompson, Z. K., Irwin, J., Charbonneau, D., et al. 2015, *Nature*, 527, 204
- Bister, M., & Emanuel, K. A. 1998, *Meteorology and Atmospheric Physics*, 65, 233
- Buckingham, E. 1914, *Physical Review*, 4, 345
- Charnay, B., Meadows, V., Misra, A., Leconte, J., & Arney, G. 2015, *The Astrophysical Journal Letters*, 813, L1
- Cowan, N. B., Greene, T., Angerhausen, D., et al. 2015, *Publications of the Astronomical Society of the Pacific*, 127, 311
- Deming, D., Seager, S., Winn, J., et al. 2009, *Publications of the Astronomical Society of the Pacific*, 121, 952
- Dressing, C. D., & Charbonneau, D. 2015, *The Astrophysical Journal*, 807, 45
- Emanuel, K. A. 1986, *Journal of the Atmospheric Sciences*, 43, 585
- Emanuel, K. A., & Bister, M. 1996, *Journal of the Atmospheric Sciences*, 53, 3276
- Emanuel, K. A., & Rotunno, R. 1989, *Tellus A*, 41, doi:10.3402/tellusa.v41i1.11817
- Fortney, J. J. 2005, *Monthly Notices of the Royal Astronomical Society*, 364, 649
- Frierson, D. M. W., Held, I. M., & Zurita-Gotor, P. 2006, *Journal of the Atmospheric Sciences*, 63, 2548
- Fromang, S., Leconte, J., & Heng, K. 2016, *Astronomy & Astrophysics*, doi:10.1051/0004-6361/201527600
- Fujii, Y., Kimura, J., Dohm, J., & Ohtake, M. 2014, *Astrobiology*, 14, 753
- Glasse, A. C. H., Bauwens, E., Bouwman, J., et al. 2010, in *Proc. SPIE 7731*, ed. J. M. Oschmann, Jr., M. C. Clampin, & H. A. MacEwen, 77310K
- Goodman, J. 2009, *The Astrophysical Journal*, 693, 1645
- Heng, K., & Kopparla, P. 2012, *The Astrophysical Journal*, 754, 60
- Heng, K., Menou, K., & Phillipps, P. J. 2011, *Monthly Notices of the Royal Astronomical Society*, 413, 2380
- Hu, R., Demory, B.-O., Seager, S., Lewis, N., & Showman, A. P. 2015, *The Astrophysical Journal*, 802, 51
- Joshi, M., Haberle, R., & Reynolds, R. 1997, *Icarus*, 129, 450
- Kaltenegger, L., & Traub, W. A. 2009, *The Astrophysical Journal*, 698, 519
- Kaspi, Y., & Showman, A. P. 2015, *The Astrophysical Journal*, 804, 60
- Kasting, J. F. 1988, *Icarus*, 74, 472
- Kasting, J. F., Whitmire, D. P., & Reynolds, R. T. 1993, *Icarus*, 101, 108
- Koll, D. D. B., & Abbot, D. S. 2015, *The Astrophysical Journal*, 802, 21
- Komacek, T. D., & Showman, A. P. 2016, *The Astrophysical Journal*, 821, 16
- Kopparapu, R. K., Wolf, E. T., Haqq-Misra, J., et al. 2016, *The Astrophysical Journal*, 819, 84
- Kreidberg, L., Bean, J. L., Désert, J.-M., et al. 2014, *Nature*, 505, 69
- Leconte, J., Forget, F., Charnay, B., et al. 2013, *Astronomy & Astrophysics*, 554, A69
- Leconte, J., Wu, H., Menou, K., & Murray, N. 2015, *Science*, 347, 632
- Li, J., & Goodman, J. 2010, *The Astrophysical Journal*, 725, 1146
- Line, M. R., & Parmentier, V. 2016, *The Astrophysical Journal*, 820, 78
- Liu, J., & Schneider, T. 2011, *Journal of the Atmospheric Sciences*, 68, 2742
- Makarov, V. V., Berghea, C., & Efroimsky, M. 2012, *The Astrophysical Journal*, 761, 83
- Matsuno, T. 1966, *Journal of the Meteorological Society of Japan. Ser. II*, 44, 25
- Menou, K. 2012a, *The Astrophysical Journal Letters*, 744, L16
- 2012b, *The Astrophysical Journal*, 745, 138
- Merlis, T. M., & Schneider, T. 2010, *Journal of Advances in Modeling Earth Systems*, 2, doi:10.3894/JAMES.2010.2.13
- Mills, S. M., & Abbot, D. S. 2013, *The Astrophysical Journal Letters*, 774, L17
- Motalebi, F., Udry, S., Gillon, M., et al. 2015, *Astronomy & Astrophysics*, 584, A72
- Owen, J. E., & Mohanty, S. 2016, *Monthly Notices of the Royal Astronomical Society*, stw959
- Parmentier, V., Showman, A. P., & Lian, Y. 2013, *Astronomy & Astrophysics*, 558, A91
- Pauluis, O. 2010, *Journal of the Atmospheric Sciences*, 68, 91
- Pauluis, O., Balaji, V., & Held, I. M. 2000, *Journal of the Atmospheric Sciences*, 57, 989
- Pauluis, O., & Held, I. M. 2002, *Journal of the Atmospheric Sciences*, 59, 125
- Peixoto, J. P., & Oort, A. H. 1984, *Reviews of Modern Physics*, 56, 365
- Perez-Becker, D., & Showman, A. P. 2013, *The Astrophysical Journal*, 776, 134
- Pierrehumbert, R. T. 2011a, *The Astrophysical Journal*, 726, L8
- 2011b, *Principles of Planetary Climate* (Cambridge University Press)
- Renno, N. O., & Ingersoll, A. P. 1996, *Journal of the Atmospheric Sciences*, 53, 572
- Robinson, T. D., & Catling, D. C. 2012, *The Astrophysical Journal*, 757, 104
- 2014, *Nature Geoscience*, 7, 12
- Seager, S., & Deming, D. 2009, *The Astrophysical Journal*, 703, 1884
- Selsis, F., Wordsworth, R. D., & Forget, F. 2011, *Astronomy and Astrophysics*, 532, 1
- Showman, A. P., Cho, J. Y.-K., & Menou, K. 2010, in *Exoplanets*, ed. S. Seager (University of Arizona Press), 471–516
- Showman, A. P., Lewis, N. K., & Fortney, J. J. 2015, *The Astrophysical Journal*, 801, 95
- Showman, A. P., & Polvani, L. M. 2011, *Astrophysical Journal*, 738, doi:10.1088/0004-637X/738/1/71
- Showman, A. P., Wordsworth, R. D., Merlis, T. M., & Kaspi, Y. 2013, in *Comparative Climatology of Terrestrial Planets*, ed. S. J. Mackwell, A. A. Simon-Miller, J. W. Harder, & M. A. Bullock, *Space Science Series* (University of Arizona Press), 277–326
- Sobel, A. H., Nilsson, J., & Polvani, L. M. 2001, *Journal of the Atmospheric Sciences*, 58, 3650
- Voigt, A., Held, I. M., & Marotzke, J. 2012, *Journal of the Atmospheric Sciences*, 69, 116
- Wordsworth, R. 2015, *The Astrophysical Journal*, 806, 180
- Yang, J., & Abbot, D. S. 2014, *The Astrophysical Journal*, 784, 155
- Yang, J., Cowan, N. B., & Abbot, D. S. 2013, *The Astrophysical Journal Letters*, 771, L45

Zalucha, A. M., Michaels, T. I., & Madhusudhan, N. 2013,
Icarus, 226, 1743